OPERATING PROCEDURES

CO_2 laser, collective scattering diagnostic at W7-AS

M. Saffman

Last Edits: 28.may 2000

Contents

Chapter 1

Safety, installation, and alignment

1.1 Safety

The CO_2 laser is a potentially dangerous radiation source. Protective goggles must always be used when working with the laser. Even if it is believed that there are no unbocked beams a stray reflection of a few percent could damage your irreplacable eyes.

In addition the laser exciter generates 10 mA of current at 30 kV, a lethal combination. Never operate the laser or exciter with the covers open unless you are well versed in safe procedures.

1.2 Startup

When turning on the system start with the receiver and then the transmitter.

1.2.1 Receiver

1. remove plastic cover on top torus window
2. turn on det. 1,2 bias to 7. mA
3. check for loose items lying around

1.2.2 Transmitter

1. shutter controller to off
2. remove plastic cover over turning mirror below the torus
3. turn on water cooler and press cooling start button on rack
4. put pick-off mirror on transmitter table up and turn on uv lamp
6. start laser (run on 9.5 mA current)
7. turn on laser stabilizer (function switch to manual (not stab))
8. turn on monitor detector bias to 10 mA
9. check that Bragg cell driver is running
(green light on right hand side of rack on)
10. verify computer is running pcanywhere: host waiting for connection or connected
11. wait 10 minutes
12. shutter controller to manual
13. open shutter and adjust stabilizer voltage for minimum noise on scope and good visual beam quality (also check spectrum on scope) 14. close shutter and put pick-off mirror down
15. make sure plexiglass covers are in-place on optical table

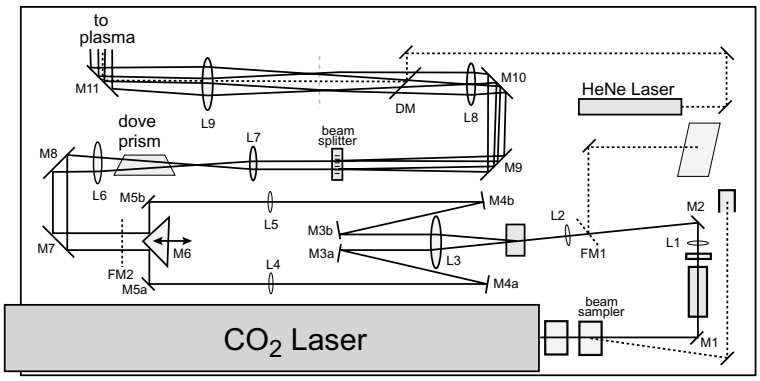

Figure 1.1: Transmitter table containing laser and beam preparation optics.

16. shutter controller to hall
17. laser stabilizer to manual and external control voltage

1.3 Shutdown

1.3.1 Transmitter

1. shutter controller to off
2. turn off laser using key
3. return laser current to 10 mA
4. turn off monitor detector bias
5. turn off scope
6. replace plastic cover on turning mirror below torus
7. turn off water cooler (wait at least 5 minutes after laser is turned off)

1.3.2 Receiver

1. replace cover on top torus window
2. turn off det. 1,2 bias

1.4 Optical alignment

This section describes how to align the optical system from laser to photodetectors. Procedures for optimizing the electronic settings in preparation for turbulence measurements are given in Sec. 2.2. The optical system comprises the transmitter table with laser and beam preparation optics, relay lenses and mirrors for sending the beams to the plasma, and a receiver table located after the plasma.

The lenses in the optical train are of ZnSe a material with low absorption losses at the CO_2 laser wavelength of 10.6 μm. The focal length of ZnSe lenses can be checked using a HeNe laser, or with visible light as follows. First determine the focal length with visible light. There are several methods: focus a far away light source onto a surface loacted a focal length behind the lens, or setup two parallel HeNe laser beams and focus them to a point that will be a focal length after the lens. Given the focal length with visible light, $f_{\rm vis}$ we can find the focal length at 10.6 μm. from the formula

$$f_{10.6} = \frac{n_{\rm vis} - 1}{n_{10.6} - 1} f_{\rm vis} \simeq 1.16 \times f_{\rm vis}$$

using the refractive indices $n_{\rm vis} = 2.624$ (589 nm) and $n_{10.6} = 2.405$.

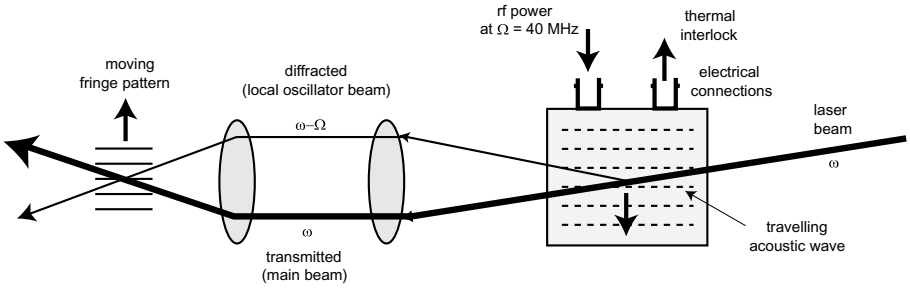

Figure 1.2: Frequency shift of beam diffracted by bragg cell.

1.4.1 Transmitter table

The transmitter table is a 2×1 m optical table mounted vertically in the basement below the W7-AS torus. The table surface is non-magnetic steel, with M6 threaded holes at 25 mm intervals. The optical layout on the transmitter table is shown in Fig. 1.1.

1.4.2 Laser

The micrometer screws on the back of the laser are used for fine adjustment of the cavity. In normal operation they rarely need to be moved. Never make fine adjustments to the cavity alignment before the laser is warmed up, which takes about 1/2 hour. Otherwise subsequent thermal motion of the cavity will change the alignment again. Complete warmup, after which the laser is relatively stable with respect to transverse mode changes can take several hours.

Using the beam pick off mirror and the stationary plate the beam quality can be checked visually. The beam should be round and symmetric, and free of hot spots. The left hand mircometer screw rotates the grating at the back of the laser which scans across the different rotational transitions. The transition giving highest output power should be chosen. Since several neighboring rotational lines have almost the same power it can be difficult to find the best one. In this case select the nominally strongest transition which has a wavelength of $\lambda = 10.59$ μm. To do so place the power meter on top of the laser near the small beam pickoff mirror. Using the narrowband filter measure the power of the peak laser lines with and without the filter. Select the line with the highest transmission through the filter. This should be about 80-85 %.

The laser has been fitted with an intracavity aperture wheel. Rotating the wheel selects different apertures. Their position is fine adjusted using scres on the side and top of the laser. Adjustment of the aperture should only be made when the laser is fully warmed up (several hours). Experience has shown that the 7.8 mm aperture gives an improved beam profile with only a few % loss in output power. The aperture marked "0" is 15 mm diameter, and has no effect on the laser mode.

As of january 1999 the laser gave about 22.5 Watts at 10 mA tube current with the 7.8 mm aperture.

1.4.3 Bragg cell

The Bragg cell is a germanium crystal with an acoustic transducer on one side. An incident beam at the Bragg angle θ_B is diffracted so that the full angle between the transmitted and diffracted beams is 75 mrad $= 2\theta_B$. The strength of the diffracted beam is proportional to the rf energy applied to the Bragg cell, while the frequency shift is determined by the rf frequency, which is nominally 40 MHz. The optical power in the diffracted (local oscillator) beams is proportional to the square of the d.c. voltage applied to the Bragg cell driver (see Zoletnik report1 of january 1999).

The sign of the frequency shift can be determined as shown in Fig. 1.2. Since the main and local oscillator beams are frequency shifted with respect to each other,

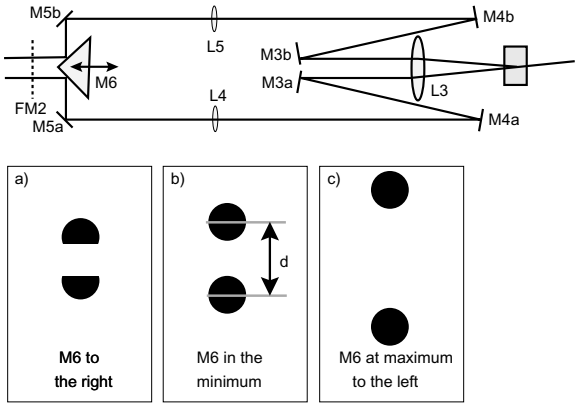

Figure 1.3: Alignment of optics for k-scans.

interfering the beams results in a moving fringe pattern. When the fringe pattern moves parallel to the fluctuations that scatter light, the registered Doppler frequency will be *downshifted* by 40 MHz, and thus centered in a band around -40 MHz. When the fringe pattern moves anti-parallel to the fluctuations that scatter light, the registered Doppler frequency will be *upshifted* by 40 MHz, and thus centered in a band around +40 MHz.

To determine the direction of fringe motion we need to know the sign of the frequency shift of the local oscillator in the Bragg cell, and the relative orientation in space of the main and local oscillator beams. The bragg cell acoustic transducer is on the side of the cell where the electrical cables are placed. The sound waves in the cell thus propagate away from the electrical cables. The optical setup is such that the incident beam copropagates with the acoustic wave, while the diffracted beam is counterpropagating with respect to the acoustic wave (along the x-axis in Fig. 1.2. The diffracted beam is thus downshifted so that its frequency is 40 MHz *lower* than that of the main beam. Note that if the Bragg cell is mechanically rotated by 180° so that the acoustical wave is propagating *up* instead of down, as in the figure, the diffracted beam would then be *upshifted* by 40 MHz.

When the beams are sent through the W7-AS torus they cross inside the torus. If the local oscillators are outside (at larger radius) the main beams below the torus, and inside the main beams above the torus then fluctuations propagating towards the center of the torus give a positive frequency shift. If the opposite is true (local oscillators are inside the main beams below the torus, and outside the main beams above the torus), then fluctuations propagating towards the center of the torus give a negative frequency shift. These two cases are referred to as positive/negative beam orientations in the shot notes.

In order to align the Bragg cell do the following.

1) Turn up the power to the cell by setting the dc bias level to 1 V.

2) Align the incident beam so it is close to the Bragg angle, and falls in the center of the window on the side of the cell.

3) Monitor the diffracted beam power while making fine adjustments to the angle of the cell using the screw on the adjustable cell holder.

4) Rotate the halfwave plate placed after the variable attenuator in order to maximize the diffracted power.

5) Repeat steps 3 and 4 iteratively to maximize the diffraction. It will be convenient to reduce the bragg cell bias voltage to avoid saturation of the diffraction, once the diffracted beam is visible. It is important that the polarization is set for maximum diffraction efficiency when measuring in order to ensure good heterodyning between the local oscillator and main beams.

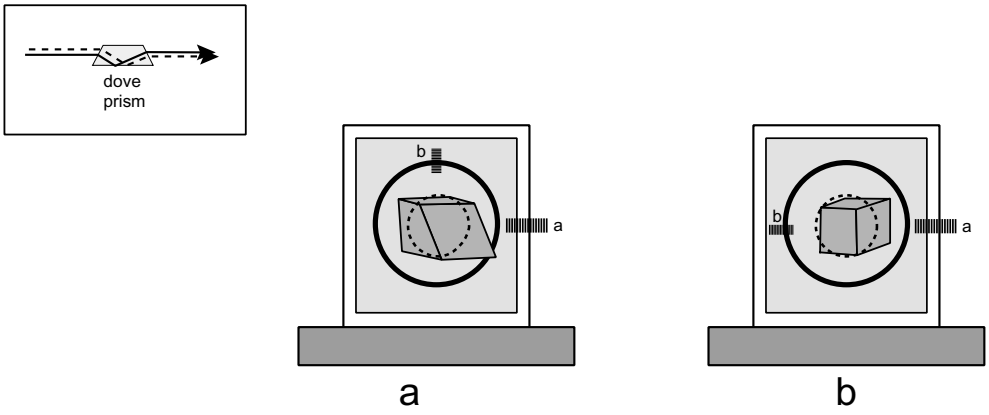

Figure 1.4: Dove prism alignment. Screw a adjusts the position of the rotating mount parallel to the table. Screw b adjusts the dove prism holder relative to the rotating mount.

1.4.4 k - Scan

The measured wavenumber is selected by moving mirror M6 which is mounted on stepper motor 1. Mirror M6 is a solid copper block in a triangular shape, with a 90° angle between the reflecting sides. Moving stepper motor 1 by 1 mm changes the beam separation after M6 by 2 mm. To correctly align the optics for wavenumber scans it is first necessary to ensure that the ring of mirrors and lenses following the Bragg cell forms a closed loop, see Fig. 1.3. Roughly align the mirrors and lenses so the main and local oscillator beams meet just past M6 when stepper motor 1 is in position 0 (all the way to the right). Adjust M3a, M3b so that the beams are centered on M4a, M4b respectively. Thereafter M3a, M3b should not be adjusted further. Then adjust M4a, M4b so that the beams are symmetric, and partially apertured by M6, as shown in inset a) in the figure. Then move stepper motor 1 several mm's to the left, so that the beams are not apertured as shown in inset b). Using a wooden ruler measure, as accurately as possible, the separation d from center to center of the beams. This measurement calibrates the measured wavenumber (given the other optical parameters, see section 2.4.4) and can be made with about 10 % accuracy. Then put flip mirror 2 (FM2) up to send the beams off the table, and observe them on an infrared plate 2-3 meters away from FM2. This procedure is dangerous, since the beams leave the table, try not to burn yourself or others, or surrounding equipment. Adjust M5a, M5b so that the beam separation measured on the distant plate is the same as that measured directly after M6. Then repeat the following steps iteratively until correct position and parallelism is obtained:

1) Move M6 all the way to the right and adjust M4a, M4b so that the beams are symmetric as in inset a) in the figure.

2) Move M6 to the left until the beam separation measured after M6 is $d = 15$ mm.

3) Raise FM2 and measured d at a distance of several meters. Then lower FM2 again.

Repeat steps 1-3 until the beams are symmetric with respect to M6 and have the same separation at both measurement locations. Three to four iterations should be sufficient. Record the separation d and the corresponding stepper motor position.

1.4.5 Dove prism

The dove prism is used to rotate the plane containing the main and local oscillator beams so that the measurement plane in the torus (selected $\mathbf{k}_{\mathrm{scat}}$ direction) is aligned correctly with respect to the toroidal magnetic field. With the normal assumption of 2D plasma turbulence we want the toroidal magnetic field to be perpendicular to the

plane containing the main and local oscillator beams. Dove prisms rotate images. A dove prism always rotates the optical field passing through it by 180° as shown in the inset of Fig. 1.4 for two parallel rays. The 180° rotation also occurs for any image. Rotating the dove prism through an angle θ rotates the beams by an angle 2θ. Once the dove prism has been aligned correctly it will rarely need readjusting. The cables connecting the dove prism to stepper motor channel 2 are therefore normally used for the diffractive beam splitter (section 1.4.6). The dove prism does not need readjustment when changing the relative position of the two measurement volumes, see Sec. 1.4.14. Furthermore when the dove prism is aligned correctly it can be used to rotate the beams about the optical axis, without displacing the beams in the (rotated) plane. To achieve this the following procedure can be used (see Fig. 1.4).

1) Make sure the beam height (plane containing the 2 beams) is exactly 4 inches above the table. Use the black plates with holes to check this.

2) Rotate the dove prism so that its base is parallel to the table surface (Fig. 1.4a). In this orientation the prism changes the beams height but not their lateral position (parallel to the table surface). Now adjust screw **b** controlling the position of the prism relative to the rotating mount so that the height of the beams after passing through the prism is unchanged. Check by rotating the prism back and forth by 180 deg.

3) Rotate the dove prism so its base is perpendicular to the table surface (Fig. 1.4b). The prism now displaces the beams parallel to the table, but does not change their vertical height. Adjust the position of the rotating mount with screw **a** so that the beams are not displaced parallel to the table after passing through the prism. Check by rotating the prism back and forth by 180°. The prism assembly should now be aligned correctly. Check by rotating the prism while watching the transmitted beams. They should rotate about the beam axis without displacement.

A potential problem with the dove prisms is that at large k values both beams only just fit through the available aperture. The beam passage should be checked over the entire k range that will be used. Fine adjustments of the beam and/or dove prism position may be necessary to avoid unwanted scattering that can lead to excessive 40 MHz leakage into the local oscillator beam.

1.4.6 Diffractive beam splitter and aperture plate

The diffractive beam splitter diffracts each beam into 2 beams with an included angle between them of 10. or 25. mrad, depending on which beam splitter is installed. About 80 % of the incident power is transferred into the two beams (40% in each), while about 20% is diffracted into higher order beams. The diffractive beamsplitter should be rotated so that the 4 beams lie in a plane when measuring with poloidal separation of the measurement volumes. The appropriate angle is marked on the diffractive beam splitter holder. Note that the diffractive beam splitter does not give a spatially symmetric deflection of the beams. One of the beams is diffracted to the side by an angle about twice larger than the diffraction angle of the other beam. This should be regarded as an error in the construction of the diffractive beam splitter, and has some consequences as regards relative alignment of the CO_2 and HeNe beams.

There is an aperture placed after the diffractive beam splitter, in its Fourier conjugate plane, that is used to block the higher order diffracted beams from propagating through the optical system. The aperture position should be adjusted so that all 4 beams (2 main and 2 local oscillator) pass through unhindered, independent of the rotation of the diffractive beam splitter.

1.4.7 HeNe alignment beam

The HeNe laser on the optical table is an aid to achieving alignment through the torus. The HeNe and CO_2 beams are combined at the dichroic plate on the laser table. The HeNe beam should be adjusted for spatial coincidence and parallel propagation with the CO_2 beams. Spatial coincidence is obtained by adjusting the HeNe mirror close to the HeNe laser while looking at all beams in the plane just after the dichroic plate.

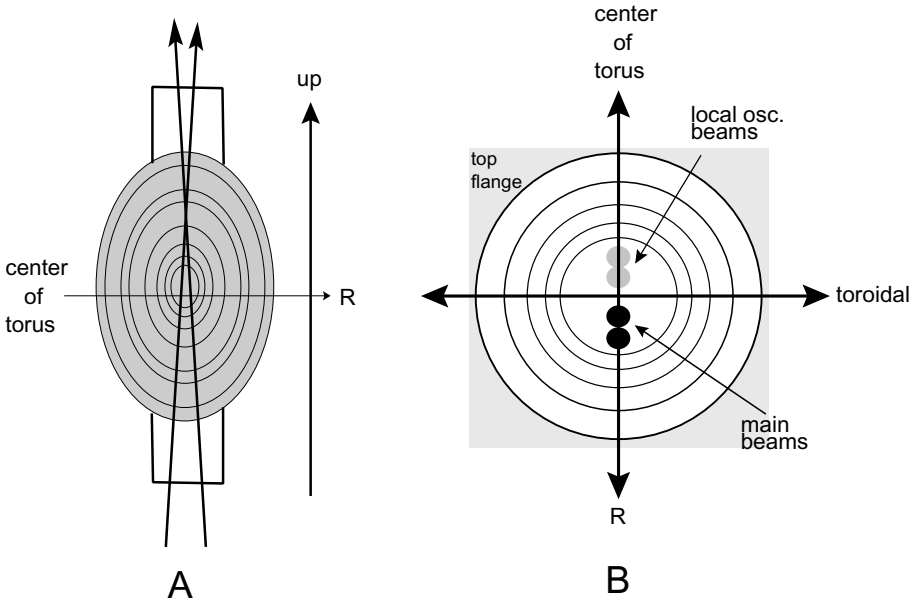

Figure 1.5: Beam alignment through the torus.

Coaxiality is obtained by adjusting the HeNe mirror closest to the dichroic plate while looking at the beams in a plane several meters away along the beam connecting the optical table with the torus. The two measurements should be repeated in alternation until satisfactory results are obtained.

When the HeNe and CO_2 beams are aligned the CO_2 beams can be blocked and the large turning mirrors and lenses on the mechanical beam used to achieve alignment of the HeNe beam through the torus. The CO_2 beams are then turned on and observed while making fine adjustments as described in the next section.

Once the He-Ne beam has been aligned with respect to the torus it should not be moved. Adjustments to the CO_2 beam can then be made, and the CO_2 beam aligned with respect to the HeNe beam using the two 3 inch turning mirrors directly before the dichroic mirror.

1.4.8 Torus alignment

It is important that the plane containing the beams as they traverse the plasma torus is perpendicular to the local B field as shown in Fig. 1.5. Assuming that the B field is nominally toroidal this implies that the beam plane should be radial. This is checked by placing a target sheet on the top flange of the lens assembly mounted on top of the machine. (Target sheets can be printed out from file ofd-plasma-2\\d:\w7as\alignment targets\target.eps. It is most useful to print the target as an overhead transparency. The sheet is then aligned with the markings on the flange and exposed to create burn marks showing the beam positions. Dove prism 1 (stepper motor 2) should then be rotated to get correct alignment, as shown in part B of the figure. Once this is achieved dove prism 2 (stepper motor 3) should be rotated to make the beams horizontal on the receiving table. The burned target sheet also serves as a quantitative record of the beam positions relative to our torus window. When making the burn marks on the target sheets ensure that the local oscillator beams are several times weaker than the main beams. In this way the relative directions of the local oscillator and main beams can be determined, which is needed to know the sign of the measured velocities (see Sec. 1.4.3).

1.4.9 Receiver table

When working on the receiver table exercise caution not to expose the detectors to excesive power levels. It is good practice to block the detectors with metal plates whenever high power beams are being aligned. The absolute maximum detector power level is 1 Watt (damage level!). The detectors have good sensitivity, and peak to peak signals of more than 1 V peak-to-peak are obtained after preamplification with optical power levels of only 1 to 2 mWatts.

1.4.10 Turning mirror

The large turning mirror transfers the vertically propagating beams from the torus to horizontally propagating beams on the table. The mirror should be adjusted to give horizontal beams at 4 " above the table surface. The black plates with predrilled holes can be used to determine accurately the 4" beam height.

1.4.11 Beam dump

The power at the beam dump can be measured by placing the Ophir power meter with 30W thermal detector head at the beam dump. The analog output from the power meter can be monitored from the control room. The calibration is 0.033 V/W.

1.4.12 Detector alignment

Completely block the main beams by placing a plate on top of the laser after the Bragg cell. The alignment is easiest to see with local oscillator powers of about 0.1 W, or higher. To prevent damage block the detectors with metal plates. Screw the beam scraper back so that the local oscillators pass freely. The first step is then to adjust the beam positions relative to the two 1" mirrors. Each beam should reflect off of a different mirror.

1. Scan stepper motor 1 between the minimum and maximum limits to be used and observe the beam motion at the lens in front of the 1" mirrors. The two beams should move horizontally while maintaining constant relative separation. Note that the maximum scan range cannot exceed the separation of the beams.
2. Put stepper motor 1 to the limit that causes the beams to translate furthest to the right. Then fine adjust the beam positions using the large turning mirror directly before the beam scraper, as well as the mirror positions such that the beams each land on different mirrors. The left-most beam should be as close as possible to the right edge of the left mirror, while maintaining good reflection from the mirror.
3. Move stepper motor 1 to the other limit. Make sure the beams still reflect off of their respective mirrors.
4. Fine adjust the large turning mirror so that the beam positions with respect to the mirrors are satisfactory at both ends of the scan.

The local oscillator power at the two detectors may not differ by more than 5 %. If this is not the case there is an alignment problem somewhere in the optical chain.

We are now ready to focus the beams onto the detectors. Put stepper motor 1 to the middle of the desired scan range. Follow the beam paths through the imaging lenses and turning mirrors and make sure the beams are well centered on the way to the detectors. It is helpful to remove the final two focusing lenses before the detectors, align the beams oughly with the detectors, and then replace the lenses to be coaxial with the beams.

For fine adjustment reduce the local oscillator power to a safe level, say about 100 mW or less and apply some ac modulation to the bragg cell driver so that the local oscillators are easily seen on the slow oscilloscope by the receiving table. Adjust the final turning mirrors before the detectors for best alignment. Verify that the ac signal seen on the scope stays fairly constant as stepper motor 1 is scanned over the desired k-scan range. If the signal is not constant follow the local oscillator beams from the beam scraper to the detectors at both limiting positions of the k-scan range to see if

the beam is being blocked somewhere. If so, try and correct by repeating the above steps. If not the problem is axial positioning of the detectors in an image plane. Try and monitor motion of the beams at the detector surface as stepper motor 1 is scanned. Move the detectors axially to minimize the observed motion.

1.4.13 Beam scraper

The beam scraper should now be adjusted to prevent the main beams from reaching the detectors as shown in Fig. **??**. First block the detectors to prevent accidental excessive exposure. Unblock the main beams on the transmitter table. Set stepper motor 1 to the low end of its range (minimum k). Move the beam scraper in, until there is no visible light from the main beams heading towards the detectors. Set stepper motor 1 to its maximum position (maximum k), and verify that there is still no main beam headed towards the detectors. It is now safe to unblock the detectors. Fine adjust the scraper position while monitoring 40 MHz crosstalk as well as a.c. modulation at the detectors. Set the scraper to maximize the ac modulation while minimizing the 40 MHz crosstalk. No single setting will be optimum for all k-scan values. It is necessary to choose a compromise setting.

1.4.14 Changing from poloidal to toroidal measurement volume separation

To change from poloidal to toroidal measurement volume separation do the following.
1. Rotate the diffractive beam splitter (stepper motor 2) by -90 degrees to the angle indicated on the beam splitter holder. The beams are now arranged in a square or rectangular pattern. The measurement volumes are now displaced vertically with respect to the optical table at the first measurement plane (plane of aperture plate).
2. Check good coincidence of He-Ne and CO_2 beams, and alignment through the torus (see Sec. 1.4.8).
3. Check that the beams are still correctly blocked at the beam scraper. If necessary fine adjust the beam scraper position at the lower limit of the k-range to be used.
4. Rotate dove prism 2 (stepper motor 3) 45 degrees. so that the two local oscillator beams are horizontally displaced after the dove prism. **When changing from poloidal to toroidal separation rotate the dove prism by** $+45^o$. **When changing from toroidal to poloidal separation rotate the dove prism by** -45^o. Note that k-scans now result in the local oscillator beams moving vertically, not horizontally as is the case for poloidal separation.

To iteratively optimize the alignment do the following.
1. Put stepper motor 1 to the middle of its k-scan range and set stepper motors 2,3 for poloidal separation.
2. Fine adjust beam alignment onto detectors for maximum ac modulation signal. Adjust only the 1" mirrors close to the detectors.
3. Rotate to toroidal separation.
4. Adjust the mirror before the dove prism for optimum detector alignment.
5. Rotate back to poloidal separation.
6. Optimize detector alignment adjusting only the 1" mirrors close to the detectors.
7. Rotate to toroidal separation.
8. Adjust the mirror before the beam dump for optimum detector alignment.
9. Rotate back to poloidal separation.

Repeat steps 2-9 until no further improvement is obtained.

1.4.15 Radial scan

The measurement volumes can be scanned radially by moving the large mirror directly below the torus. This requires realignment of the subsequent lenses and mirrors. .....

1.5 Cables

1.5.1 Transmitter rack to receiver table

There are BNC, data and power cables. These are:

cable	function
coax 1	det. 1 signal
coax 2	det. 2 signal
coax 3	3 kHz + DC bias from receiver rack to Bragg cell driver
coax 4	video signal from receiver table / beam dump power meter
coax 5	24 V for warning lamps
twisted pair	shutter control from receiver table
serial cable	stepper motor dcontrol cable 1
serial cable	stepper motor control cable 2

1.5.2 Transmitter rack to control room

There are 5 BNC cables between the control room and the large rack by the laser. These are: As more than 5 different signals are sometimes used some of the cables have multiple functions in the list below.

cable	function
5	Ch. 2 detector signal to control room
6,7	enable loop for hall interlock laser shutter control
8	video camera
11	monitor detector signal to control room
12	Laser stabilizer voltage from control room (0-6V gives 0-1 kV)
13	laser shutter control (open/closed) from control room
14	Ch. 1 detector signal to control room
15	d.c. level from power meter at beam dump
16,17	trigger signal loop to control room for manual trigger

Chapter 2

Running the experiment

2.1 General procedures

Start by turning on the optical system at the transmitter and receiver as described in section 1.2.
The computers are used for the following tasks:

ofd-plasma-1:
The ofd-plasma-1 machine should be running pcanywhere "waiting for a connection" so that it can be controlled from ofd-plasma-2. Data acquisition runs on ofd-plasma-1, see section 2.4. It is convenient to save acquired data directly to the ofd-plasma-4 disk so that data inspection can be done on ofd-plasma-4 without additional file transfers.

ofd-plasma-2:
remote control of ofd-plasma-1 through pcanywhere
recording of shot note information in file \\ofd-plasma-2\d:\w7as\info\shotnotes.xls

ofd-plasma-4:
display of shot information by eXceed connection to das4, and display of nmul program evaluation of new data using fortran plot program and/or idl programs

At the end of the day shut down the optical system following the procedure in section 1.3. It is a good idea to transfer the days data files to the afs file system (see section 3.2) so that there will be sufficient disk space on ofd-plasma-1 and ofd-plasma-4 the following shot day.

2.2 Optimizing the detection parameters

The basic procedures for aligning the optical system were described in Sec. 1.4. Before actually measuring it is necessary to find optimum settings for the bragg cell and photodetectors. The bragg cell drive voltage, and hence local oscillator power, should in general be set as high as possible without damaging the detectors or overloading the A/D converters. Either damage or overload can be the limiting factor depending on the amount of 40 MHz leakage in the optical chain. Note that the maximum input level of the A/D converters (with 0 dB electronic gain) is 2 $V_{\rm pp}$ or +10 dBm. By varying the electronic gain input signals in the range of +12.7 to -27.3 dBm can be mapped onto the full range of the A/D converters. A table of dBm conversions is given in section 5.2.

When changing the bragg cell drive voltage measure the local oscillator beam powers and verify that excessive power is never sent to the detectors for any stepper motor 1 position. The local oscillator power is proportional to the square of the dc voltage sent to the Bragg cell.

sm 1 [mm]	$\mathcal{P}_{\text{beam dump}}$	$\mathcal{P}_{\text{loc.osc.1}}$	$\mathcal{P}_{\text{loc.osc.2}}$	relative sensitivity	(relative sensitivity)^2
3.	4.1	.003	.005	.21	.04
3.5	4.6	.007	.008	.33	.11
4.	5.0	.012	.013	.46	.21
5.	5.5	.027	.028	.71	.51
6.	5.7	.051	.050	1.0	1.0
7.	5.76	.079	.075	1.3	1.56
8.	5.79	.101	.098	1.4	2.0
9.	5.75	.114	.112	1.5	2.3
10.	5.79	.122	.120	1.6	2.4

Table 2.1: k-scan correction factors measured on 29.january 1999. The relative sensitivity factor is calculated using the local oscillator power of channel 1. Measured data are normalized by *dividing* by the factors given in the table.

Some recommended typical settings as of 30.january 1999 are:

laser current 8 mA.
laser power $\sim$ 20 W
power at beam dump $\sim$ 5.5 W
bragg cell drive voltage = 0.2 V
This gives about 100 mW /channel local oscillator power, depending on the **k** setting (stepper motor 1). The electronic gain should then be set as high as possible without overloading the A/D card. It should be possible to have at least 10 dB gain. If not there may be a problem with the optical alignment causing excessive 40 MHz leakage.
Check raw data levels for different gain settings. If one of the channels has significantly lower raw signal levels it can be compensated by raising the electronic gain on that channel accordingly.

2.3 k-scan correction factor

When doing k-scans the main beam and local oscillator powers change with the stepper motor position as shown in Table 2.1 . This leads to a k dependent correction factor that should be applied to the measured data. As is seen from Eq. (4.47) the electrical signal due to a given turbulence level in the plasma is proportional to $\sqrt{\mathcal{P}\mathcal{P}_{\text{lo}}}$, where $\mathcal{P}$ is the power of the main beam and $\mathcal{P}_{\text{lo}}$ is the power of the local oscillator. We can thus define a normalization factor based on the variation in beam powers as stepper motor 1 is scanned. Note that power spectra are proportional to the square of the electrical voltage, and should thus be normalized by the square of the relative sensitivity. This is listed in the last column of Table 2.1.

The k-scan correction factors may change with realignment of the optical system. They should be rechecked periodically.

2.4 Acquiring quadrature data

For detailed information about the quadrature card and software see ofd-plasma-2\\d:\w7as\programs\quadcard'

1. connect to ofd-plasma-1 from ofd-plasma-2 using pcanywhere

2. start d:\w7as\programs\quadcard\qdm4.exe.

3. In acquisition menu open “setup the acquisition”.

4. In setup window select clock-external, trigger-external and BCN test-disabled. Select buffer size in bytes (see below for length of recorded data vs. buffer size), electronic

gains, and check save after acquisition. Select a boot file and load it.

The choices are:

direct sampling mode: stream.ttf max. clock rate is 42 Ms/sec
stream2.ttf max. clock rate is 85 Ms/sec
stream4.ttf max. clock rate is 170 Ms/sec

quadrature sampling mode: filt24_1.ttf decimation by 4
filt26_1.ttf decimation by 6

clock	**boot filter**	**frq. Range**	**MB for 1 sec. of data**
int.(64 MHz)	stream	NOT A VALID MODE	> 84
int.(64 MHz)	stream2	0-16 MHz	64
int.(64 MHz)	stream4	0-8 MHz	32
ext.(160 MHz)	stream	NOT A VALID MODE	> 84
ext.(160 MHz)	stream2	NOT A VALID MODE	> 84
ext.(160 MHz)	stream4	0-20 MHz	80
ext.(160 MHz)	filt24	-8 - 8 MHz	80
ext.(160 MHz)	filt26	-6 - 6 MHz	54

5. Select an output file name. To save data directly to ofd-plasma-4 use S:\w7as\data:.. for the output file path.

6. Click the acquire now box. The program is now waiting for data. The acquire now box has a gray check next to it to indicate that the program is waiting for an acquisition. No changes can be made to the setup screen until the acquisition is completed, at which time the gray check will disappear.

7. Click on the "..." box to select a new output file name. There may be a delay while the previous data is being written to disk. When the program is ready the "select destination for buffer write" box will appear.

Repeat steps 6 and 7 for each shot.

See the end of section 1.4.13 for information on how to optimize the local oscillator and electronic gain settings.

At the end of the day, or during the day as needed, ftp raw data files to andrew file system to make space on ofd-plasma-1 disk. Use /afs/ipp-garching.mpg.de/m/saffman/w7as/data directory. Transfer with windows file manager or explorer or ftp (binary not ascii ftp transfer).

2.4.1 Stepper motors

The stepper motors are controlled by a 3 channel Advantech PCL-839 card sitting in a ISA bus slot. The program step.exe provides control of the stepper motors under windows NT. This program requires the PCL839 driver to be loaded.

2.4.2 Fortran data viewing program

For information on Fortran plot program see the file ofd-plasma-2\\D:\w7as\programs\fortranplot\plot_program.ps .

2.4.3 IDL data analysis programs

IPP has a site license for IDL including NT computers. To access it start X:\i386_nt35\bin\idl.lnk.
See the information on the web page http:/ /www.rzg.mpg.de/rzg/graphics/graphics_NT.html

concerning how to activate the license.

The data analysis routines written by Sandor Zoletnik are located in ofd-plasma-2\\D:\w7as\programs\idl\ For information on using the routines see the file ofd-plasma-2\\D:\w7as\info\ report1.ps.

(old info Marks program) To make pictures from time/frequency output of plot program use the following.

psd.idl creates x-y line plots of power spectrum

tf.idl creates 2D color density plots of power spectrum vs. shot time

Naming convention is: data file shxxx.dat is processede by plot to give tfxxx.dat

psd : tfxxx.dat -¿ psdxxx.eps

tf: tfxxx.dat -¿ tfxxx.eps

2.4.4 Optics programs

beamcad program can be used for proagation of gaussian beams

OpticalBeamDiameters.nb is a Mathematica program that calculates beam diameters and spacings, as well as measured wavenumbers.

2.4.5 NMUL

Log on to das4 and run nmul to see shot info

2.5 W7-AS timing sequence

Trigger	Specification	ON-Time (sec)	OFF- Time
Ts	Timer start 0		
Tm		25.0	
OH	Tm+0.450	25.450	Tm+ 1350 msec
NBI	NBI trigger (T0-4)	31.0	
Mstart	Magnetic field start	31.5	
Td	Trigger Td	32.0	
MF5	Td+0.001	32.001	Td+5920 msec
TF	Td+0.100	32.1	TD+5820 msec
BZ	Td+0.021	32.021	TD+6500 msec
T0	Pulse start, Trigger T0	35.0	
Pende	Pulse finished	< 38.0	
Te	Pulse program ende	45.0	

Chapter 3

Computer and software information

3.1 PC computer information

The experiment uses 4 computers with intel processors running Windows NT. ofd-plasma-1 is located in the rack by the transmitter table and is used for digital data acquisition and stepper motor control. ofd-plasma-2 is in the control room and is used for remotre control of ofd-plasma-1, as well as the primary source for documentation of the experiment. ofd-plasma-3 is a laptop used for control of ofd-plasma-1 from the receiver table during alignment work. It also doubles as an extra office computer. ofd-plasma-4 is in the control room and is used for data analysis and display of shot data via X-window access to das4.

ofd-plasma-1 130.183.60.25
transmitter table rack in experiment hall
Windows NT/95
Pentium 133 MHz, 128 MB, 4 GB
drives C,D

ofd-plasma-2 130.183.60.26
control room
Windows NT
Pentium 133 MHz, 64 MB, 5 GB
drives C,D,E

ofd-plasma-3 130.183.60.27
laptop for receiving table, office
Windows NT
Pentium 133 MHz, 32 MB, 1.3 GB
drives C,D

ofd-plasma-4 130.183.60.29
control room
Windows NT
Pentium II 450 MHz, 132 MB, 8.5 GB
drives C,D
There is a CD-rom burner for recording data, etc.

3.1.1 Remote control

Data acquisition is executed on ofd-plasma-1. It is therefore necessary to direct the operation of this machine from the control room. To do so pcanywhere32 software from Symantec is used. ofd-plasma-1 acts as a host, and any of the other machines perform remote control through a client connection. In order to provide control from unix remote shell service software is being installed on ofd-plasma-1. The rsh daemon from Denicomp, inc. appears to function adequately. A trial version is currently installed, with a registered version planned for december 98/january 99.

3.2 File locations

Generally speaking the directory structures are similar on all 4 ofd machines. Master versions of all information and program files are kept on ofd-plasma-2. Versions on other machines should not be considered as primary versions.

ofd-plasma-1	
D:\w7as\info\	info files
	shot notes
	(copies from ofd-plasma-2, not masters)
D:\w7as\programs\	
dma_.exe	data acquisition program
step_.exe	stepper motor program
plot_.exe	plot program
\quadcard\	dma boot filters, etc. are also kept here
	(copies from ofd-plasma-2, not masters)
D:\w7as\data	data storage

ofd-plasma-2	
	master versions of all information and program files
D:\w7as\info\	operating procedures (master version)
	shot notes (master version)
D:\w7as\programs\	data acquisition and analysis porograms
The following subdirectories contain:	
\fortranplot\	NT program for viewing data and calculating spectra, correlations
\idl\marksprograms\	primitive idl routines for making plots
	using output data from fortran program
\idl\	extensive idl routines
\optics\	mathematica program for optics calculations
\Power_meter\	basic program for reading power meter
\quadcard\	data acquisition program and boot filters
\stepmotor\	program for moving stepper motors
D:\w7as\data	data storage
E:\w7as\data	additional data storage

ofd-plasma-3	
C:\w7as\info	info files, shot notes
C:\w7as\programs step_xx.exe	stepper motor program
plot_.exe	plot program

In order to facilitate file sharing and transfer between NT computers disk mappings are used. The following drive names are used uniformly on all the computers.

mapped drive	physical drive	description
K	\\ofd-plasma-1\OP1-C	
L	\\ofd-plasma-1\OP1-D	
M	\\ofd-plasma-2\OP2-C	
N	\\ofd-plasma-2\OP2-D	
O	\\ofd-plasma-2\OP2-E	
P	\\ofd-plasma-3\OP3-C	
Q	\\ofd-plasma-3\OP3-D	
R	\\ofd-plasma-4\OP4-C	
S	\\ofd-plasma-4\OP4-D	
T	\\ofd-plasma2a\OP3-C	(laptop on D2 subnet)
U	\\ofd-plasma2a\OP3-D	(laptop on D2 subnet)
X	\\cdserv\afsipp	IPP software repository
Y	\\cdserv\saffman	Y:\m\w7as\data\..... points to the data on afs tape

On machines running NT 4.0 service pack 3 there may be password trouble when attempting to connect to cdserv. If so one needs to make the following setting in the registry. Add a parameter to the key HKEY_LOCAL_MACHINE\system\currentcontrolset\services\rdr\parameters. It should be called EnablePlainTextPassword and make it a DWORD with value 1.

3.3 PC network setup

For help with PC networking see Josef Maier. Josef.maier@ipp-garching.mpg.de

TCP/IP addresses are:

ofd-plasma-1	130.183.60.25
ofd-plasma-2	130.183.60.26
ofd-plasma-3	130.183.60.27
ofd-plasma-4	130.183.60.29

The following NT network services should be installed. They may not all be necessary, but eveything works with this list.

Computer browser
Microsoft TCP/IP printing
NetBIOS interface
RPC configuration
Server
Simple TCP/IP services
SNMP service
Workstation

Configure TCP/IP protocol with:

subnet	255.255.255.0
gateway	130.183.60.240
domain name server	w7.ipp-garching.mpg.de
	130.183.60.91
	130.183.1.21
domain suffixes	ipp-garching.mpg.de
	ipp.mpg.de
	rzg.mpg.de
wins primary	130.183.1.51
wins secondary	130.183.51.103
enable DNS for windows resolution	

The office is on the D2 subnet. When putting the laptop in the office change network settings to

ofd-plasma2a	130.183.1.185
subnet	255.255.255.0
gateway	130.183.1.29
domain name server	ipp-garching.mpg.de
	130.183.1.21
	130.183.60.91
domain suffixes	w7.ipp-garching.mpg.de
	ipp.mpg.de
	rzg.mpg.de
wins primary	130.183.1.51
wins secondary	130.183.51.103
enable DNS for windows resolution	

All 4 ofd machines are set up to allow access to afs through cdserv. To access cdserv it is convenient, but not necessary, to log on to the ipp domain when logging on to NT. Account saffman can be used, with the same password as for account saffman on afs, or establish your own IPP NT domain account. To do so see Josef Maier.

3.4 Network printers

An easy way to connnect to network printers from NT machines is to make LPR ports.

Print server	servus1.w7
printer	hp34 (control room)
	col8
	col8t
	etc...

3.5 Unix machines

At IPP Unix machines administer and provide email, afs disks, and cdserv service. Our data is stored under account saffman on afs. The password for this account is available from mark.saffman@risoe.dk.

A local unix machine is das4.w7.ipp-garching.mpg.de 130.183.62.84 . There are many others. The passwords on das4 are administered centrally so changing the password for account saffman on das4 should change it for afs access.

A central machine is cdserv.rzg.mpg.de 130.183.9.20 .

3.6 Tape backup

Large tape storage space on afs is in directory

/afs/ipp-garching.mpg.de/m/saffman/w7as/data

smaller disk backup is

/afs/ipp-garching.mpg.de/u/saffman/w7as/data

When accessing files from tape backup it may be necessary to "prefetch" them. To do so use the command (from UNIX)

/afs/ipp/@sys/bin/fs prefetch *.* (where *.* is the file(s) to be prefetched)

to check prefetch status

/afs/ipp/@sys/bin/fs getres *.*

If access is denied when trying to look at /afs/ipp-garching.mpg.de/m/saffman try the following:

Login to uts.ipp-garching.mpg.de
login saffman
passwd
run kinit saffman
password

Run quota to see storage limits

Our current limits are 100 GB of data and 5000 file names. Usage as of november 1998 was 56 GB and 3000 file names.

Chapter 4

Technical guide

4.1 Mode spectrum of the CO_2 laser

This section was prepared by Nils Plesner Basse.

4.2 Optical Prerequisites

We are using a Gaussian beam formalism, as this provides a good approximation to the transverse modes of a resonator with finite diameter mirrors.

4.3 Rudiments of Laser Theory(S1.4)

In a laser, one encloses a volume of excited material in an optical cavity. I am dealing with a CO_2 laser. Photons are reflected back and forth between two mirrors to obtain stimulated emission af light.

The laser amplification coefficient $\alpha_m(\omega)$ is defined as:

$$-\alpha(\omega) \equiv \alpha_m(\omega) = \frac{\lambda^2 \gamma_{\mathrm{rad}}}{4\pi\Delta\omega_{\mathrm{a}}} \frac{\mathrm{N}_1 - \mathrm{N}_2}{1 + [2(\omega - \omega_{21})/\Delta\omega_{\mathrm{a}}]^2}$$

Here, λ is the transition wavelength, γ_{rad} the radiative decay rate of the transition, $\Delta\omega_a$ the transition linewidth, $N_1 - N_2$ the population difference (atoms per unit volume); finallly, ω_{12} is the transition frequency between two energy levels E_1 and E_2 of the atoms.

4.4 The CO_2 Laser(D5.4.1)

The radiation from this type of laser has a wavelength of 10.6 μm. This is due to the vibrational transition $(v_1, v_2^l, v_3) = 00^01 \rightarrow 10^00$. Here, l is the angular momentum quantum number.

Brewster-angle end windows are placed at the ends of the discharge tube in order to transmit linearly polarised light. The Brewster-angle is defined as $\tan\theta_B = \frac{\mathrm{n_2}}{\mathrm{n_1}}$, where n_1 and n_2 are refraction indices. The choice of this angle leads to a minute reflection loss.

4.5 A Stable Half-Symmetric Resonator(S19.1,19.2)

In a half-symmetric resonator, one mirror is plane, while the other is curved. A radius of curvature is defined for each mirror. Assuming R_1 is this curvature for the plane mirror, $R_1 = \infty$. The curvature of the other mirror is finite, in my case $R_2 = 3$ m. The condition that the wavefront curvature of a gaussian beam must be equal to the mirror curvature at the mirror leaves us three equations:

$$R(z_1) = z_1 + \frac{\mathrm{z_R^2}}{\mathrm{z_1}} = -R_1 \qquad R(z_2) = z_2 + \frac{\mathrm{z_R^2}}{\mathrm{z_2}} = +R_2 \qquad L = z_2 - z_1$$

$z_R = \frac{\pi \mathrm{w_0^2}}{\lambda}$, the 'Rayleigh range', is the distance from the beam waist to where the beam diameter has increased by $\sqrt{2}$.

The gaussian curvature is defined as positive for a diverging beam, negative for a converging beam, travelling to the right.

Solving the first two equations for $z_{1,2}$ one arrives at:

$$z_1 = \frac{-\mathrm{R_1} \pm \sqrt{\mathrm{R_1^2 - 4z_R^2}}}{2} \qquad z_2 = \frac{+\mathrm{R_2} \pm \sqrt{\mathrm{R_2^2 - 4z_R^2}}}{2}$$

Furthermore, using the last equation we solve for z_R^2:

$$z_R^2 = \frac{\mathrm{L(R_1 - L)(R_2 - L)(R_2 + R_1 - L)}}{(R_2 + R_1 - 2L)^2}$$

We will define 'resonator g parameters':

$$g_1 \equiv 1 - \frac{\mathrm{L}}{\mathrm{R_1}} \qquad g_2 \equiv 1 - \frac{\mathrm{L}}{\mathrm{R_2}}$$

Utilising the fact that

$$R_1 = \frac{\mathrm{L}}{1 - \mathrm{g_1}} \qquad R_2 = \frac{\mathrm{L}}{1 - \mathrm{g_2}}$$

the Rayleigh range squared can be expressed as:

$$z_R^2 = \frac{\mathrm{g_1 g_2 (1 - g_1 g_2)}}{(\mathrm{g_1 + g_2 - 2 g_1 g_2})^2} L^2$$

Inserting this into our solutions for $z_{1,2}$ the spot sizes at the ends of the resonator are:

$$w_1^2 = \frac{\mathrm{L}\lambda}{\pi} \sqrt{\frac{\mathrm{g_2}}{\mathrm{g_1(1 - g_1 g_2)}}} \qquad w_2^2 = \frac{\mathrm{L}\lambda}{\pi} \sqrt{\frac{\mathrm{g_1}}{\mathrm{g_2(1 - g_1 g_2)}}}$$

We have in the above used:

$$w_{1,2} \equiv w(z_{1,2}) = w_0 \sqrt{1 + (\frac{\mathrm{z_{1,2}}}{\mathrm{z_R}})^2}$$

Finally, the waist spot size (in our case at the plane mirror in the cavity) is given by:

$$w_0^2 = \frac{\mathrm{L}\lambda}{\pi} \sqrt{\frac{\mathrm{g_1 g_2 (1 - g_1 g_2)}}{(\mathrm{g_1 + g_2 - 2 g_1 g_2})^2}}$$

For completeness,

$$\psi(z) = \tan^{-1}(\frac{\mathrm{z}}{\mathrm{z_R}})$$

In our case L = 1.6 m, so $g_1 = 1$ and $g_2 = 0.47$. This means that the stability criterion of a cavity, $0 \leq g_1 g_2 \leq 1$, is fulfilled, the product being slightly less than one half.

Furthermore, w_0 is about 2.25 mm.

4.6 Axial Frequency Spacing(S1.6)

The steady-state oscillation condition for a linear laser cavity of length L is:

$$\frac{\varepsilon_2}{\varepsilon_1} = r_1 r_2 e^{(2\alpha_m L_m - \frac{2\mathrm{j}\omega\mathrm{L}}{\mathrm{c}})} = 1$$

The $\frac{\varepsilon_2}{\varepsilon_1}$ term is the total round-trip gain (beginning with ε_1, ending with ε_2). The coefficients r_1 and r_2 are the wave-amplitude reflections, α_m is the laser amplification coefficient, L_m is the length of the laser-gain medium and the signal wave has frequency ω. Thus, the exponential terms can be interpreted as follows:

$e^{(2\alpha_m L_m)}$ is the round-trip voltage amplification and

$e^{\frac{-2\mathrm{j}\omega\mathrm{L}}{\mathrm{c}}}$ is the round-trip phase shift.

The phase shift must be equal to unity, or equivalently, to $e^{-jq2\pi}$. This enforces the equality

$$\frac{2\omega\mathrm{L}}{\mathrm{c}} = q2\pi, q = \text{integer}$$

or

$$\omega = \omega_q = 2\pi\nu_q \equiv 2\pi q(\frac{\mathrm{c}}{2\mathrm{L}})$$

This means that the longitudinal cavity modes are spaced as

$$\Delta\nu \equiv \nu_{q+1} - \nu_q = \frac{\mathrm{c}}{2\mathrm{L}}$$

For the CO_2 laser

$$\Delta\nu \approx 94 \text{ MHz}$$

4.7 The Paraxial Wave Equation(S16.1)

The scalar wave equation:

$$[\nabla^2 + k^2]\tilde{E}(x, y, z) = 0$$

$$\tilde{E}(x, y, z) \equiv \tilde{u}(x, y, z)e^{i(kz-\omega t)}$$

,where $\tilde{u}$ describes the transverse profile of the beam.

Assuming that the z-dependence of $\tilde{u}$ is slow compared to the transverse variations of the beam, we arrive at the paraxial wave equation:

$$\frac{\partial\tilde{\mathrm{u}}(\bar{\mathrm{s}}, \mathrm{z})}{\partial\mathrm{z}} = \frac{\mathrm{i}}{2\mathrm{k}}\nabla_t^2\tilde{u}(\bar{s}, z)$$

The Laplacian ∇_t^2 is acting on the transverse plane, and $\bar{s} \equiv (r, \theta)$ or (x,y) determines whether one uses cylindrical or rectangular coordinates, respectively.

4.7.1 Solution in Rectangular Coordinates(S16.4)

In rectangular coordinates, the paraxial wave equation takes on the following guise:

$$\frac{\partial^2\tilde{\mathrm{u}}}{\partial\mathrm{x}^2} + \frac{\partial^2\tilde{\mathrm{u}}}{\partial\mathrm{y}^2} - 2jk\frac{\partial\tilde{\mathrm{u}}}{\partial\mathrm{z}} = 0$$

The problem now is to conjure up the Hermite-gaussian eigensolutions $\tilde{u}_{nm}(x, y, z)$.

Writing

$$\tilde{u}_{nm}(x, y, z) = \tilde{u}_n(x, z)\tilde{u}_m(y, z)$$

we see that we can solve the transverse coordinate equations independently.

We bravely bring forth the ansatz:

$$\tilde{u}_n(x,z) = A(\tilde{q}(z))h_n(\frac{\mathrm{x}}{\tilde{\mathrm{p}}(\mathrm{z})})e^{-jk\frac{x^2}{2\tilde{\mathrm{q}}(\mathrm{z})}}$$

,where A, $\tilde{p}$ and h_n are initially unknown functions and

$$\tilde{q} = \tilde{q}(z) = \tilde{q}_0 + z - z_0$$

is the complex curvature of the wave (also defined as: $\frac{1}{\tilde{\mathrm{q}}(\mathrm{z})} \equiv \frac{1}{\mathrm{R}(\mathrm{z})} - j\frac{\lambda}{\pi \mathrm{w}^2(\mathrm{z})}$) , leading to the fact that $\frac{\mathrm{d}\tilde{\mathrm{q}}}{\mathrm{dz}} = 1$.

After som hair-raising but nevertheless trivial algebra the full solution is dragged out of the equations:

$$\tilde{u}_n(x,z) = \mathcal{C}(\frac{\tilde{\mathrm{q}}_0}{\tilde{\mathrm{q}}})^{\frac{1}{2}}(\frac{\tilde{\mathrm{q}}_0\tilde{\mathrm{q}}^*}{\tilde{\mathrm{q}}\tilde{\mathrm{q}}_0^*})^{\frac{\mathrm{n}}{2}}H_n(\frac{\sqrt{2}\mathrm{x}}{\mathrm{w}(\mathrm{z})})e^{-j\frac{\mathrm{kx}^2}{2\tilde{\mathrm{q}}(\mathrm{z})}}$$

,where $\mathcal{C} = (\frac{2}{\pi})^{\frac{1}{4}}(\frac{1}{2^{\mathrm{n}}(\mathrm{n}!)\mathrm{w}_0})^{\frac{1}{2}}$, H_n are the Hermite polynomials and $\tilde{u}_n(x,z)$ obeys

$$\int_{-\infty}^{\infty} |\tilde{u}_n(x,z)|^2 dx = 1$$

To conclude, the free-space Hermite-gaussian TEM_{nm} solutions including the plane-wave e^{-jkz} phase-shift factor is:

$$\tilde{u}_n(x,z) = \mathcal{C}(\frac{\tilde{\mathrm{q}}_0}{\tilde{\mathrm{q}}})^{\frac{1}{2}}(\frac{\tilde{\mathrm{q}}_0\tilde{\mathrm{q}}^*}{\tilde{\mathrm{q}}\tilde{\mathrm{q}}_0^*})^{\frac{\mathrm{n}}{2}}H_n(\frac{\sqrt{2}\mathrm{x}}{\mathrm{w}(\mathrm{z})})e^{-j\frac{\mathrm{kx}^2}{2\tilde{\mathrm{q}}(\mathrm{z})}-jkz}$$

4.7.2 The Guoy Phase Shift(S16.4)

The Guoy phase shift is a term used for the phenomenon that a beam travelling through a focal region will experience a phase shift. If the lowest-order gaussian mode has a phase shift of $\psi(z) \equiv \tan^{-1}(\frac{\pi \mathrm{w}^2(\mathrm{z})}{\mathrm{R}(\mathrm{z})\lambda})$ at a plane z measured relative to the focal plane, an nm-th order Hermite-gaussian mode will have a phase shift of (n+m+1) $\psi(z)$. The difference in shifts leads to different resonance frequencies and mode beats of different nm-th order modes.

4.8 Transverse Modes(S19.3)

To have modes, we require that the total round-trip phase shift is an integer multiple of 2π. This shift is given by

$$kL - (n+m+1)\cos^{-1}[\pm\sqrt{g_1 g_2}] = q\pi, q = \text{integer}$$

$$\Longleftrightarrow$$

$$\nu_{nmq} = \frac{\mathrm{c}}{2\mathrm{L}}[q + \frac{(\mathrm{m}+\mathrm{n}+1)}{\pi}\cos^{-1}[\pm\sqrt{g_1 g_2}]]$$

,where $\psi(z_2) - \psi(z_1) = \cos^{-1}[\pm\sqrt{g_1 g_2}]$ (+ for $g_{1,2} > 0$, - for $g_{1,2} < 0$).

In our case, $\cos^{-1}\sqrt{0.47} = 0.8$. Choosing q = 0,

$$\nu_{nm0} = \frac{\mathrm{c}(\mathrm{m}+\mathrm{n}+1)}{2\mathrm{L}\pi}\cos^{-1}[\pm\sqrt{g_1 g_2}]$$

For example,

$$\nu_{000} = 24 \text{ MHz} \qquad \nu_{100} = \nu_{010} = 49 \text{ MHz}$$

The signal of a laser oscillating in two modes can be written

$$\varepsilon(x,y,t) = \tilde{u}_1(x,y)e^{j\omega_1 t} + \tilde{u}_2(x,y)e^{j\omega_2 t}$$

The total photocurrent is

q_1	n_1	m_1	q_2	n_2	m_2	Beat(MHz)
0	0	0	0	1	0	24
0	0	0	0	0	1	24
0	0	0	0	1	1	49
0	0	0	0	1	2	73
0	0	0	0	2	1	73
0	0	0	1	0	0	94
0	0	0	1	1	0	118 (24)
0	0	0	1	0	1	118 (24)
0	0	0	1	1	1	142 (49)
0	0	0	1	1	2	167 (73)
0	0	0	1	2	1	167 (73)
0	1	0	1	0	0	69
0	0	1	1	0	0	69
0	1	1	1	0	0	45
0	1	2	1	0	0	21
0	2	1	1	0	0	21
1	0	0	0	2	2	4
1	0	0	0	3	2	28

Table 4.1: Hermite-gaussian mode mixing

$$i(t) = \int\int |\varepsilon(x,y,t)|^2 dxdy$$

$$= I_{01} + I_{02} + I_{12}\cos[(\omega_2 - \omega_1)t + \phi_{12}]$$

,where $\omega_2 - \omega_1$ is the beat frequency.

In general, we obtain:

$$\nu_2 - \nu_1 = \Delta q \Delta\nu_{ax} + \Delta(n+m)\Delta\nu_{trans}$$

, where $\Delta q = q_2 - q_1$, $\Delta n = n_2 - n_1$, $\Delta m = m_2 - m_1$, $\Delta\nu_{ax} = 94$ MHz and $\Delta\nu_{trans} = 24$ MHz.

Two beating frequencies are observed at approximately 5 and 20 MHz.

Choosing $q_1 = q_2 = 0$ the first beats are

24 MHz 49 MHz 73 MHz

respectively.

Observing two entries of Table 4.1, the measured 20 MHz beating frequency might be a result of those mode beats.

The penultimate entry in Table 4.1 could be the measured 5 MHz beat.

4.9 Aperturing(S17.5)

We would like our laser to oscillate exclusively in the TEM_{00} mode. This can be accomplished by placing a circular aperture at the plane mirror in the laser cavity to suppress the higher-order modes.

If the diameter of the aperture is large enough to let higher modes pass, one observes the so-called 'donut mode', which is a lit ring with a dark spot on axis, hence the nickname. As astigmatism (an asymmetry where $\tilde{q}(z), w(z)$ and $\psi(z)$ are different for the x and y coordinates) is introduced by the Brewster windows in the laser, the donut mode stems from a linear combination of the $TEM_{01}\binom{O}{O}$ and the $TEM_{10}(OO)$ modes.

If one uses the peak of the ripple of the outermost Hermite-gaussian pattern, x_n, as the half-width of the function, one has the approximate relationship

$$x_n \approx w\sqrt{n}$$

Placing an aperture of diameter 2a in the laser cavity, only those Hermite-gaussian modes with $x_n \leq a$ will oscillate with low losses. The equivalent of this condition is that

$$n \leq N_{max} \approx (\frac{\mathrm{a}}{\mathrm{w}})^2$$

,which is most accurate for a $\gg w$.

* * *

If we want to calculate the transmitted power through an aperture of radius a, it is convenient to use cylindrical coordinates. The solution to the paraxial equation is expressed as Laguerre-Gaussian modes, where the transverse profile of the beam is:

$$\tilde{u}_{pm}(r,\theta,z) =$$
$$\sqrt{\frac{2\mathrm{p}!}{(1+\delta_{0\mathrm{m}})\pi(\mathrm{m}+\mathrm{p})!}}\frac{\mathrm{e}^{\mathrm{j}(2\mathrm{p}+\mathrm{m}+1)(\psi(\mathrm{z})-\psi_0)}}{\mathrm{w(z)}}(\frac{\sqrt{2}\mathrm{r}}{\mathrm{w(z)}})^m L_p^m(\frac{2\mathrm{r}^2}{\mathrm{w}^2(\mathrm{z})})e^{-jk\frac{\mathrm{r}^2}{2\mathrm{q(z)}}+im\theta}$$

; L_p^m are the associated Laguerre polynomials, p ≥ 0 is the radial index and m $\leq$ p is the azimuthal mode index.

For example,

$$L_0^0(x) = 1 \qquad L_1^1(x) = -1 \qquad L_2^1(x) = 2x-4 \qquad L_2^2(x) = 2$$

Taking the norm square yields:

$$|\tilde{u}_{pm}(r,\theta,z)|^2 =$$
$$\frac{2\mathrm{p}!}{(1+\delta_{0\mathrm{m}})\pi(\mathrm{m}+\mathrm{p})!}\frac{1}{\mathrm{w}^2(\mathrm{z})}(\frac{\sqrt{2}\mathrm{r}}{\mathrm{w(z)}})^{2m}[L_p^m(\frac{2\mathrm{r}^2}{\mathrm{w}^2(\mathrm{z})})]^2 e^{\frac{-2\mathrm{r}^2}{\mathrm{w}^2(\mathrm{z})}}$$

The transmitted power is:

$$P(z) = \int\int |\tilde{u}|^2 dA = \int_0^a \int_0^{2\pi} |\tilde{u}_{pm}(r,\theta,z)|^2 d\theta dr$$

The first four norm square beam profiles are:

$$|\tilde{u}_{00}|^2 = \frac{1}{\pi\mathrm{w}^2(\mathrm{z})}e^{\frac{-2\mathrm{r}^2}{\mathrm{w}^2(\mathrm{z})}} \qquad |\tilde{u}_{11}|^2 = \frac{2\mathrm{r}^2}{\pi\mathrm{w}^4(\mathrm{z})}e^{\frac{-2\mathrm{r}^2}{\mathrm{w}^2(\mathrm{z})}}$$
$$|\tilde{u}_{21}|^2 = \frac{4\mathrm{r}^2}{3\pi\mathrm{w}^4(\mathrm{z})}(\frac{4\mathrm{r}^2}{\mathrm{w}^2(\mathrm{z})}-4)^2 e^{\frac{-2\mathrm{r}^2}{\mathrm{w}^2(\mathrm{z})}} \qquad |\tilde{u}_{22}|^2 = \frac{8\mathrm{r}^4}{3\pi\mathrm{w}^6(\mathrm{z})}e^{\frac{-2\mathrm{r}^2}{\mathrm{w}^2(\mathrm{z})}}$$

The phase shift is as described in the 'Transverse Modes' section, except for the fact that (m+n+1) is replaced by (2p+m+1).

As can be seen from the above table, the $q_1 = 0, m_1 = 1, p_1 = 1$ and $q_2 = 1, m_2 = 0, p_2 = 0$ beat is 21 MHz. We now investigate the power ratio between these two low modes.

The power for these modes are:

$$P_{00}(a) = \frac{2}{\mathrm{w}^2(\mathrm{z})}\int_0^a e^{\frac{-2\mathrm{r}^2}{\mathrm{w}^2(\mathrm{z})}}dr \qquad P_{11}(a) = \frac{4}{\mathrm{w}^4(\mathrm{z})}\int_0^a r^2 e^{\frac{-2\mathrm{r}^2}{\mathrm{w}^2(\mathrm{z})}}dr$$

The fraction $\frac{\mathrm{P_{11}(a)}}{\mathrm{P_{00}(a)}}$ is therefore

$$\frac{2\int_0^{\mathrm{a}} \mathrm{r}^2 \mathrm{e}^{\frac{-2\mathrm{r}^2}{\mathrm{w}^2(\mathrm{z})}}\mathrm{dr}}{\mathrm{w}^2(\mathrm{z})\int_0^{\mathrm{a}} \mathrm{e}^{\frac{-2\mathrm{r}^2}{\mathrm{w}^2(\mathrm{z})}}\mathrm{dr}}$$

q_1	m_1	p_1	q_2	m_2	p_2	Beat(MHz)
0	0	0	0	1	0	24
0	0	0	0	0	1	49
0	0	0	0	1	1	73
0	0	0	0	1	2	122 (28)
0	0	0	1	0	0	94
0	0	0	1	1	0	118 (24)
0	0	0	1	0	1	142 (49)
0	0	0	1	1	1	167 (73)
0	0	0	1	1	2	215 (28)
0	1	0	1	0	0	69
0	0	1	1	0	0	45
0	1	1	1	0	0	21
1	0	0	0	0	2	4 (3.6)

Table 4.2: Laguerre-gaussian mode mixing

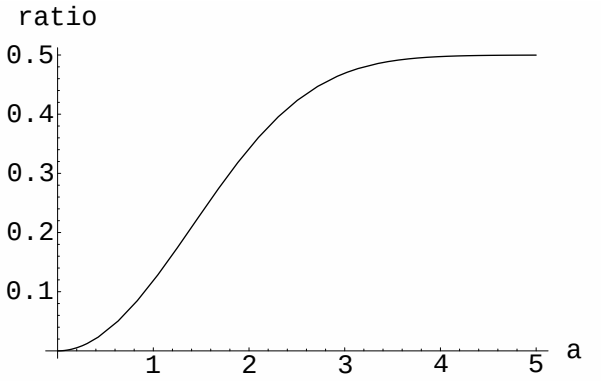

Figure 4.1: $\frac{P_{11}(a)}{P_{00}(a)}$ as a function of the aperture radius a in mm.

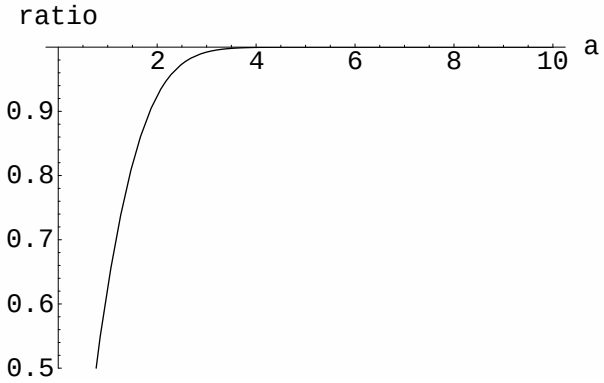

Figure 4.2: $\frac{\mathrm{P_{00}(a)}}{\mathrm{P_{00}(\infty)}}$ as a function of the aperture radius a in mm.

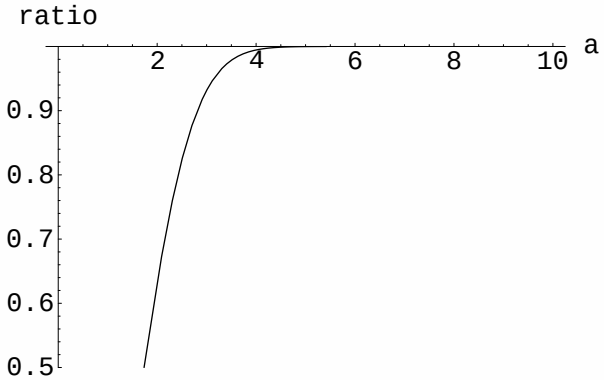

Figure 4.3: $\frac{\mathrm{P_{11}(a)}}{\mathrm{P_{11}(\infty)}}$ as a function of the aperture radius a in mm.

This can be calculated numerically in for example Mathematica. We set $w(z) = w(z_0) = 2.25$ mm. For aperture radii a = 3.5, 3.75 and 4.0 mm (the sizes available) the ratio is roughly constant at 0.5. So, the transmitted power of the 11-mode is only half that of the 00-mode. The ratio decreases rapidly for a less than 3 mm, as can be seen from Figure 4.1.

One can analyse this result further by looking at the ratios

$$\frac{\mathrm{P_{00}(a)}}{\mathrm{P_{00}(\infty)}} = \frac{\int_0^{\mathrm{a}} \mathrm{e}^{\frac{-2\mathrm{r}^2}{\mathrm{w}^2(\mathrm{z})}}\mathrm{dr}}{\int_0^{\infty} \mathrm{e}^{\frac{-2\mathrm{r}^2}{\mathrm{w}^2(\mathrm{z})}}\mathrm{dr}} \text{ and } \frac{\mathrm{P_{11}(a)}}{\mathrm{P_{11}(\infty)}} = \frac{\int_0^{\mathrm{a}} \mathrm{r}^2\mathrm{e}^{\frac{-2\mathrm{r}^2}{\mathrm{w}^2(\mathrm{z})}}\mathrm{dr}}{\int_0^{\infty} \mathrm{r}^2\mathrm{e}^{\frac{-2\mathrm{r}^2}{\mathrm{w}^2(\mathrm{z})}}\mathrm{dr}}$$

,where $\int_0^{\infty} e^{\frac{-2\mathrm{r}^2}{\mathrm{w}^2(\mathrm{z})}} dr = \frac{\mathrm{w(z)}}{2}\sqrt{\frac{\pi}{2}}$ and $\int_0^{\infty} r^2 e^{\frac{-2\mathrm{r}^2}{\mathrm{w}^2(\mathrm{z})}} dr = (\frac{\mathrm{w(z)}^2}{2})^{\frac{3}{2}}\frac{\sqrt{\pi}}{4}$. See Figures 4.2 and 4.3.

The 4 (3.6) MHz beat is investigated in Figure 4.4.

$$\frac{\mathrm{P_{20}(a)}}{\mathrm{P_{00}(a)}} = \frac{\int_0^{\mathrm{a}} \mathrm{e}^{\frac{-2\mathrm{r}^2}{\mathrm{w}^2(\mathrm{z})}}(\frac{4\mathrm{r}^4}{\mathrm{w}^4(\mathrm{z})} - \frac{8\mathrm{r}^2}{\mathrm{w}^2(\mathrm{z})} + 2)\mathrm{dr}}{\int_0^{\mathrm{a}} \mathrm{e}^{\frac{-2\mathrm{r}^2}{\mathrm{w}^2(\mathrm{z})}}\mathrm{dr}}$$

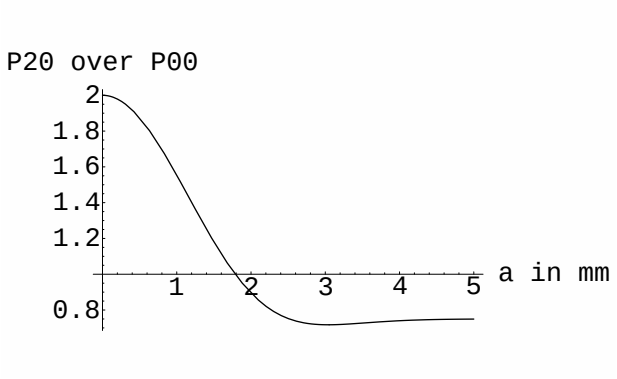

Figure 4.4: $\frac{P_{20}(a)}{P_{00}(a)}$ as a function of the aperture radius a in mm.

4.10 Light scattering

Some relevant considerations about light scattering are given in this section.

4.11 Refractive index of a plasma

The refractive index of a plasma is given by

$$n = \sqrt{1 - \frac{\omega_p^2}{\omega^2}}, \tag{4.1}$$

where ω_p is the plasma frequency and ω is the frequency of the electromagnetic radiation. Using Eq. (5.1), and expanding the electron density as $n_e = n_{e0}(1 + \delta n_e)$ we have

$$n \simeq 1 - \frac{e^2 n_{e0}}{2\epsilon_0 m_e \omega^2} - \frac{e^2 n_{e0}}{2\epsilon_0 m_e \omega^2}\delta n_e. \tag{4.2}$$

We can thus write perturbations to the index of refraction in the form

$$\delta n = \beta \delta n_e, \tag{4.3}$$

where $\beta = -e^2 n_{e0}/(2\epsilon_0 m_e \omega^2)$. Using a CO_2 laser with wavelength 10.6 μm, and assuming a background plasma density characteristic of a fusion experiment, $n_{e0} = 10^{20}$, β takes the numerical value of $5. \times 10^{-6}$. Thus refractive index perturbations in a plasma are very weak.

Under conditions of weak scattering propagation through the plasma can be described without resorting to multiple scattering theory. The condition can be estimated as follows. The phase perturbation seen by the optical beam on propagating through a density perturbation δn_e of size a is given by

$$\delta\phi = ka\delta n = ka\beta\delta n_e, \tag{4.4}$$

where $k = 2\pi/\lambda$ is the optical wavenumber. The mean of δn_e is zero so we should consider the squared fluctuations,

$$(\delta\phi)^2 = (ka\beta\delta n_e)^2. \tag{4.5}$$

The expected phase deviation on traversing a region of size L, assuming normally distributed fluctuations in the small eddies of size a is then

$$\begin{aligned}\Delta\phi &= \sqrt{\sum_1^N (\delta\phi)^2} \\ &= \sqrt{\frac{L}{a}}\delta\phi, \end{aligned} \tag{4.6}$$

where we have used L/a for the expected number N of eddies. In the heterodyne measurement configuration we select eddies of size $a \sim \Lambda$, where $\Lambda \simeq \lambda/\theta$ is the fringe spacing created by crossing the beams at angle θ. The phase shift is then

$$\Delta\phi = \sqrt{L\Lambda}\, k\beta\delta n_e. \tag{4.7}$$

In typical experiments on fusion plasmas we have $L \sim 1.$ m, $\Lambda \sim 10^{-3}$ m, and $\delta n_e \sim 10^{-3}$. We then find

$$\Delta\phi \sim 10^{-4}. \tag{4.8}$$

Neglecting multiple scattering is thus a good approximation.

4.12 Collective scattering with gaussian beams

We will now invoke the weak scattering limit (first Born approximation) to calculate the light scattered from a laser beam upon propagation through a plasma. The time independent wave equation describing linear propagation in an inhomogeneous medium is [see (**??**)]

$$\frac{\partial\mathcal{E}}{\partial z} - \frac{i}{2k_0}\nabla_\perp^2\mathcal{E} = ik_0 n_1\mathcal{E}, \tag{4.9}$$

where $\mathcal{E}$ is the slowly varying envelope of the optical field, $k_0 = \omega_0(1+\beta)/c$ and $n_1(\mathbf{r}) = \beta\delta n_e$.

Consider the case of a plasma with a sinusoidal density modulation leading to a spatially dependent refractive index

$$n_1 = n_{10}\cos(\kappa x). \tag{4.10}$$

When the plasma is uniform $n_1 = 0$ and (4.9) has gaussian beam solutions $\mathcal{E} = A_g(x,y,z)$ that satisfy $\partial A_g/\partial z - (1/2k_0)\nabla_\perp^2 A_g = 0$. We will therefore seek solutions in the presence of inhomogeneities in the form

$$\mathcal{E} = A_g(x,y,z)\left[f(z) + f_+(z)e^{\imath(k_\perp x - k_\perp^2/2k_0 z)} + f_-(z)e^{\imath(-k_\perp x - k_\perp^2/2k_0 z)}\right], \tag{4.11}$$

where $k_\perp$ is a transverse wavenumber that will be fixed by phasematching arguments. Equation (4.9) then gives

$$\begin{aligned}&\frac{df}{dz} + \frac{df_+}{dz}e^{\imath(k_\perp x - k_\perp^2/2k_0 z)} + \frac{df_-}{dz}e^{\imath(-k_\perp x - k_\perp^2/2k_0 z)} \\ &= i\frac{k_0 n_{10}}{2}(e^{\imath\kappa x} + e^{-\imath\kappa x})(f + f_+e^{\imath(k_\perp x - k_\perp^2/2k_0 z)} + f_-e^{\imath(-k_\perp x - k_\perp^2/2k_0 z)}). \end{aligned} \tag{4.12}$$

Taking a Fourier transform in x gives

$$\begin{aligned}&\delta(q)\frac{df}{dz} + \delta(q+k_\perp)\frac{df_+}{dz}e^{\imath(-k_\perp^2/2k_0 z)} + \delta(q-k_\perp)\frac{df_-}{dz}e^{\imath(-k_\perp^2/2k_0 z)} \\ &= i\frac{k_0 n_{10}}{2}(\delta(q+\kappa) + \delta(q-\kappa))f + [\delta(q+\kappa+k_\perp) + \delta(q-\kappa+k_\perp)]\, f_+e^{\imath(-k_\perp^2/2k_0 z)} \\ &+ [\delta(q+\kappa-k_\perp) + \delta(q-\kappa-k_\perp)]\, f_-e^{\imath(-k_\perp^2/2k_0 z)}, \end{aligned} \tag{4.13}$$

where q is the transform variable. Setting $k_\perp = \kappa$ and equating terms with the same argument of the delta function gives a set of ordinary differential equations for the z dependent amplitudes f_i. They read

$$\frac{df}{dz} = i\gamma(f_+ + f_-)e^{-\imath k_d z}, \tag{4.14}$$

$$\frac{df_+}{dz} = \frac{df_-}{dz} = i\gamma f e^{\imath k_d z}, \tag{4.15}$$

$$\tag{4.16}$$

where the diffraction wavenumber is $k_d = k_\perp^2/(2k_0)$ and $\gamma = k_0 n_{10}/2$. In addition the terms proportional to $\delta(q \pm 2\kappa)$ give formally $f_\pm = 0$. We will simply ignore these additional constraints, the justification being that they correspond to scattering into the next higher order. The scattering is weak and proportional to the small parameter $\Delta\phi$ and we expect terms of next higher order to be proportional to $(\Delta\phi)^2$ and thus negligible.

When the sidebands $f_\pm$ are zero at the entrance to the scattering region the set (4.16) has the solutions

$$f(z) = f(0)e^{-\imath\frac{k_d}{2}z}\left[\cos\left(\frac{k_d s}{2}z\right) + \frac{i}{s}\sin\left(\frac{k_d s}{2}z\right)\right], \tag{4.17}$$

$$f_+(z) = f_-(z) = f(0)\frac{2i\gamma}{k_d s}e^{\imath\frac{k_d}{2}z}\sin\left(\frac{k_d s}{2}z\right), \tag{4.18}$$

where $s = \sqrt{1 + 8\gamma^2/k_d^2}$.

These results imply a sinusoidal redistribution of the energy from the input beam to the sidebands, and back again. We should recall, however, that the assumption of weak scattering was used in the derivation so that the above equations should only be used in the limit where $k_d s L/2 \ll 1$, where L is the propagation distance. The scattered power in the sideband is then given by

$$\frac{P_+}{P_0} = \gamma^2 L^2, \tag{4.19}$$

where P_0 is the power of the incident gaussian beam. Note that the scattered power is independent of the diameter of the Gaussian beam. Indeed Eq. (4.19) applies equally well to a lowest order TEM_{00} beam as well as to a higher order Gaussian type beam.

It's instructive to rewrite (4.19) in terms of the classical radius of the electron r_e (see Eq. (**??**)) in which case we find

$$\frac{P_+}{P_0} = \pi\frac{L^2}{k_0^2}(\pi r_e^2)(n_{e0}\ \delta n_e)^2. \tag{4.20}$$

Let's check the region of validity of this formula[1] for scattering of 10 μm light from cm scale fluctuations in a strongly perturbed fusion plasma. We thus take

$$\begin{aligned} k_0 &= \frac{2\pi}{10^{-5}}\ [m^{-1}], \\ k_\perp &= \frac{2\pi}{10^{-2}}\ [m^{-1}], \\ n_{e0} &= 10^{20}\ [m^{-3}], \\ \delta n_e &= 10^{-2}. \end{aligned} \tag{4.21}$$

We then have $k_d = 0.31$ m^{-1}, $\gamma = 0.016$ m^{-1}, $s = 1.01$, and $L_{\max} \sim 2/k_d s \sim 6$ m. A scattering length of $L \sim 0.5$ m and an incident power of $P_0 \sim 1$ W gives a scattered power of about 0.6×10^{-4} W. More difficult conditions corresponding to measurements at W7-AS might be $L \sim 0.2$ m, $n_{e0} \sim 10^{18}$ m^{-3}, $\delta n_e \sim 10^{-3}$, and $P_0 \sim 10$ W which gives $P_+ \sim 10^{-10}$ W.

[1] Note, for example, that in the book by Hutchinson Eq. (4.20) appears with an additional factor of 1/2 on the right hand side. The discrepancy should be checked.

4.13 Spatial resolution

4.14 Spatially localized scattering with an inhomogeneous magnetic field

In fusion plasmas the toroidal magnetic field is considerably stronger than the other components. This leads to a primarily two-dimensional turbulence in the plane perpendicular to the magnetic field. Since the field direction varies in space the orientation of the plane within which the turbulent fluctuations lie also varies in space. This effect can be exploited to give spatially localized measurements in a region considerably shorter than the extent of the overlap of the main and local oscillator beams. We will evaluate this approach to localized using a three dimensional formulation of the scattering problem.

Following the treatment given in section 4.12 the main and local oscillator beams satisfy

$$\frac{\partial \mathcal{E}_m}{\partial z} - \frac{i}{2k_0}\nabla_\perp^2 \mathcal{E}_m = ik_0 n_1 \mathcal{E}_m, \tag{4.22}$$

$$\frac{\partial \mathcal{E}_{lo}}{\partial z} - \frac{i}{2k_0}\nabla_\perp^2 \mathcal{E}_{lo} = ik_0 n_1 \mathcal{E}_{lo}, \tag{4.23}$$

where

$$\mathcal{E}_m = A_g(x,y,z) f_m(z) e^{i(k_\perp x - k_\perp^2/2k_0 z)} \tag{4.24}$$

$$\mathcal{E}_{lo} = A_g(x,y,z) f_{lo}(z) e^{i(-k_\perp x - k_\perp^2/2k_0 z)}, \tag{4.25}$$

and

$$\partial A_g/\partial z - (1/2k_0)\nabla_\perp^2 A_g = 0.$$

We consider a sinusoidal modulation of the plasma density, and hence the refractive index, along an arbitrary direction κ in space:

$$n_1 = n_{10}\cos(\kappa \cdot \mathbf{r}). \tag{4.26}$$

... not finished

4.14.1 CO_2 collective scattering in plasmas

There have been many measurements of plasma turbulence using collective scattering with a CO_2 laser. This note summarizes some of those results and the experimental parameters that were used. This should give some insight into why we have insufficient signal levels at W7-AS.

A number of relevant works, and their parameters are given in Table 4.3.

Some possible measurement volume parameters for the Risø diagnostic are given in Table 4.4.

By way of reference we estimate that in W7-AS $k_\mathrm{D} \sim 900$ [cm^{-1}] whereas we have attempted to measure at $\kappa \sim 140$ [cm^{-1}]

4.15 Photodetection and signal to noise ratio

4.15.1 Thermal noise

Let's start by recalling some basics about useful systems of units and the background thermal noise level of electrical components. It is convenient to introduce a logarithmic scale for measuring electrical quantities. Thus a given power level can be described on a logarithmic scale as a number of decibels or dB, defined by the relation

	year	machine	method	laser power [W]	spot diameter [cm]	axial res. [cm]	κ [cm^{-1}]	[
Surko and Slusher[1]	1976	ATC	FS	200	0.7 FWHM		2.5-25	
Surko and Slusher[2]	1980	Alcator A	CB-FFS	100	0.3		0-30	
Meyer and Mahn [3],[4]	1981	W7-A	FS	35	0.6 (waist?)		125	
Fahrbach et al. [5]	1981	INTEREX	FS	50	?		40-240	1
Truc et al.[6]	1982	TRF	FS	2	2		8-14	
Evans et al.[7]	1983	TOSCA	FFS	2.5	0.48		1-8	
Hellermann and Holzhauer[8]	1984	WASAKI	FFS	10	0.8		11-57	3
Devynck et al.[9]	1993	TORE S.	FS	4.5	5.4		3-15	

Table 4.3: Collective scattering turbulence measurements in large scale fusion plasmas using cw 10.6 μm radiation. (FS = forward scattering, FFS = far forward scattering, CB-FFS = crossed beam far forward scattering)

κ [cm^{-1}]	Λ [cm]	α	d [cm]	L$_z$ [cm]	θ	$d_{\rm lens}$ [cm]	$D_{\rm lens}$ [cm]
30	.21	4.8	.6	119	.005	.25	.56
60	.10	2.4	.3	30	.01	.49	1.1
100	.06	1.4	.2	12	.02	.74	1.9

Table 4.4: Measuring volume parameters for $\lambda = 10.6$ μm, and $\lambda_{\rm Debye} = 70$ μm ($k_{\rm Debye} = 900$ cm^{-1}). The parameters are scattering wave number κ, fringe spacing $\Lambda = \lambda/\theta$, Salpeter parameter $\alpha = 1/\kappa\lambda_{\rm Debye}$, Gaussian measuring volume diameter d, axial length of measuring volume $L_z = d/\theta$, full angle between beams θ, corresponding beam diameter in Fourier plane of lens ($f = 1.1M$) $d_{\rm lens}$, and corresponding beam separation in Fourier plane $D_{\rm lens}$.

$$dB \equiv 10 \log_{10} P, \tag{4.27}$$

where P is the power. Equation (4.27) defines a relative scale so that the relation between two power levels P_1 and P_2 measured in dB is simply $10 \log_{10} P_1/P_2$.

An absolute power scale is often needed. Therefore the notation dBm has been introduced, where dBm are simply dB's referenced to a power level of 1 mW. Thus a power P measured in dBm is

$$P[dBm] \equiv 10 \log_{10} \frac{P[\mathrm{W}]}{0.001}. \tag{4.28}$$

Unless explicitly written otherwise it is always assumed that dBm refer to a *power* and not a voltage or current level.

Let's now specialize to 50 Ω systems. The root mean square or rms power load on a resistor R is $P = RI^2 = V^2/R$, where I and V are the rms current and voltage respectively. Thus the power load on a 50 Ω resistor can be written in terms of the rms currents and voltages as

$$P_{50\Omega} = 47. + 10 \log_{10} I^2_{\rm rms} \quad [\mathrm{dBm}], \tag{4.29}$$

$$= 13. + 10 \log_{10} V^2_{\rm rms} \quad [\mathrm{dBm}]. \tag{4.30}$$

We can always express these relations in terms of peak to peak waveforms ($f(t) = (f_{\rm pp}/2) \cos \omega t$) using $f_{\rm pp} = 2\sqrt{2} f_{\rm rms}$.

Electrical components at temperature T exhibit noise due to the random thermal excitation of charges. This is known as Johnson or Nyquist noise, or simply thermal noise. Unless other noise sources are larger the thermal noise sets a lower limit to the detection of weak signals. A detector of resistance R generates a flat noise spectrum (white noise) with a rms power level

		Units	no. 5467	no. 5541	no. 5300
type			PCI-L-3	PCI-L-3	PCI-L
test date			14.11.1995	14.11.1995	23.08.1994
test conditions					
temperature	T	K	293	293	296
detector area	A_d	m^2	1×10^{-6}	1×10^{-6}	1×10^{-6}
bias current	I_b	mA	10	10	20
chopper frequency		Hz	397	397	400
optical power	$\mathcal{P}$	W	0.002	0.002	0.0015
test results					
signal voltage	V	μV	3000	2500	2600
vol. responsivity	$\mathcal{R}_v$	V / W	1.5	1.25	1.7
noise density		nV / $Hz^{1/2}$	1.1	1.25	1.55
detectivity	D^*	cm $Hz^{1/2}$ /W	1.3×10^8	$1. \times 10^8$	1.1×10^8
detector resistance	R_d	Ω	52	53	73
derived results					
noise figure		dB	1.65	2.76	4.63
NEP (1 MHz BW)	NEP	W	7.7×10^{-7}	$1. \times 10^{-6}$	9.1×10^{-7}
photoconductive gain	G		5.5×10^{-3}	4.5×10^{-3}	4.5×10^{-3}

Table 4.5: Detector parameters. The derived results are calculated from the supplied data assuming $\lambda = 10.6$ μm and a quantum efficiency $\eta = 0.6$. The noise figure is the excess detector noise relative to the ideal thermal noise of a resistor with the same resistance as the detector.

$$P_{\rm th} = 4k_BTB, \tag{4.31}$$

where k_B is Boltzmann's constant and B is the measurement bandwidth. Equivalently we can write

$$I_{\rm th}^2 = \frac{4k_BTB}{R} \tag{4.32}$$

and

$$V_{\rm th}^2 = 4k_BTRB. \tag{4.33}$$

Assuming a room temperature of 300 K we note that $k_BT = 0.026$ eV $= 4.16 \times 10^{-21}$ J and the thermal noise power is given by

$$P_{\rm th} = -167.8 + 10\log_{10} B[\text{Hz}] \text{ dBm}. \tag{4.34}$$

This is generally a small number: the thermal noise power in room temperature 50Ω systems in a 1 MHz bandwidth is about -114. dBm. Equivalently the thermal noise density is 0.91 nV/$Hz^{1/2}$.

4.15.2 Detector characteristics

The CO_2 laser scattering system uses photoconductive HgCdTe detectors of type PCI-L-3 from Vigo Systems Ltd. These are room temperature devices with an active area of 1 mm^2. The damage threshold of these detectors is 100 W/cm^2, so the maximum input power should not exceed 1 W. Relevant data from the test sheets delivered with the detectors are shown in Table 4.5.

The detector electronics are shown in Fig. 4.5. The detectors are biased using a load resistor of $R_L = 950$ Ω. The voltage across the detector resistance R_d is amplified by a Perry Amplifier model 490. It is a 50 Ω device (input and output impedance) with 26 dB of gain over a bandwidth of 1 kHz to 100 MHz, and a noise figure of 2.8 dB. The maximum output level is 3 V_{pp}.

Following the preamp there is a Minicircuits ??? 48 MHz low pass filter, and then a Boston Electronics 493A/40 wide band amplifier with 40 dB gain in a bandwidth of 1

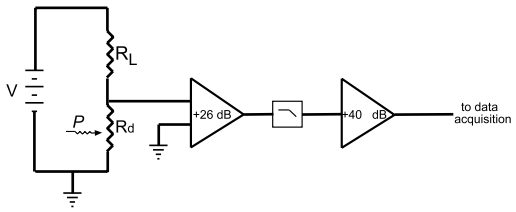

Figure 4.5: Detector electronics.

kHz to 500 MHz. The 493A/40 has a maximum output of 5 V_{pp} and an input noise of 50 μV rms, wideband. This translates into an input noise power in the full bandwidth of -73. dBm, or -83. dBm in a 50 MHz bandwidth. Since the first stage 26 dB preamp amplifies its input thermal noise (+ noise figure) to a level of -62. dBm in a 50 MHz bandwidth the noise at the input to the second preamp is completely negligible. Finally, following the 2^{nd} preamp there is a Boston Electronics 491 video line driver with unity gain.

Given the above data the noise level seen at the output of the detector/preamp assemblies should be the thermal limit increased by the noise figures of the detector and the first stage preamp, and amplified by the total gain. This translates to a noise level using the Hameg HM5005 spectrum analyzer 250 kHz bandwidth setting of about -43. dBm. This level agrees to within 1-2 dB of baseline measurements done at W7-AS in november '98. There is no noticeable increase of the noise level when the detector bias current is increased from 0 to 10 mA.

4.15.3 Photodetection

The scattering diagnostic is based on a heterodyne detection scheme where a strong local oscillator is mixed with the weak signal due to scattering from the plasma. To understand why a simpler direct detection scheme is not practical for this experiment we need to account for the noise processes associated with photodetection.

The current responsivity $\mathcal{R}_i$ of the detector is defined by

$$\mathcal{R}_i = \frac{\mathcal{I}}{\mathcal{P}}, \tag{4.35}$$

where $\mathcal{I}$ is the photogenerated current and $\mathcal{P}$ is the optical power illuminating the detector[2]. The photogenerated current is given by

$$\mathcal{I} = e\eta \frac{\mathcal{P}}{h\nu} G, \tag{4.36}$$

where e is the electronic charge, η is the quantum efficiency of the detector, h is Planck's constant, ν is the optical frequency, and G is the photoconductive gain. The photoconductive gain is a dimensionless quantity given by $G = \tau/\tau_{tr}$ where τ is the lifetime of a photogenerated charge carrier, and τ_{tr} is the transit time across the device. Since the transit time depends on the applied electric field the gain increases with bias current. See, for example, Dereniak and Boreman[10] for a detailed discussion. Using Eqs. (4.35,4.36) we have

$$\mathcal{R}_i = \frac{e\eta}{h\nu} G. \tag{4.37}$$

The voltage responsivity is then given by

$$\mathcal{R}_v = R_{eq}\mathcal{R}_i = \frac{e\eta}{h\nu} G R_{eq}, \tag{4.38}$$

where $R_{eq} = R_d R_L/(R_d + R_L)$ is the equivalent resistance of the detector and load resistors in parallel. Note that the responsivity is proportional to the product ηG, and

[2] We will generally use calligraphic type face for optical quantities.

it would be necessary to measure additional characteristics of the carrier transport in the device in order to determine separate values of η and G. We have assumed that $\eta = 0.6$ in order to calculate the photoconductive gain given in Table 4.5. While the photoconductive gain of cooled devices can be much larger than unity, operation at room temperature decreases the carrier lifetime, and hence the gain.

In a direct detection experiment the signal to noise ratio of the resulting electronic signal power is

$$z = \frac{\mathcal{I}^2}{I_{\rm th}^2 + I_{\rm gr}^2 + I_{\rm pa}^2 + I_{\rm 1/f}^2}, \tag{4.39}$$

where

$$I_{\rm th}^2 = \frac{4k_BTB}{R_{\rm eq}}, \tag{4.40}$$

$$I_{\rm gr}^2 = 4{\rm e}^2G^2B\left(\eta\frac{\mathcal{P}+\mathcal{P}_{\rm bg}}{h\nu} + g_{\rm th}\right), \tag{4.41}$$

$$I_{\rm pa}^2 = \frac{4k_BTB}{R_{\rm eff,pa}}, \tag{4.42}$$

are the thermal, generation recombination, and preamplifier noise powers respectively, and $I_{\rm 1/f}^2$ is the $1/f$ noise. In the above $\mathcal{P}_{\rm bg}$ is the optical power due to background radiation, $g_{\rm th}$ is the thermal (phonon assisted) generation rate of charge carriers, and $R_{\rm eff,pa}$ is the noise effective input impedance of the preamplifier[3]. Since we will be working at an intermediate frequency of 40 MHz the $1/f$ noise can be assumed negligible. Equation (4.39) can then be rewritten in the form

$$z = \frac{1}{4B}\frac{{\rm e}^2G^2g^2}{\frac{k_BT}{R_{\rm eff}} + {\rm e}^2G^2\left(g + g_{\rm bg} + g_{\rm th}\right)}, \tag{4.43}$$

where $R_{\rm eff} = R_{\rm eq}R_{\rm eff,pa}/(R_{\rm eq} + R_{\rm eff,pa})$ is the combined noise effective impedance of the detector, the load resistor, and the preamplifier, $g = \eta\mathcal{P}/h\nu$ is the carrier generation rate due to the signal, and $g_{\rm bg} = \eta\mathcal{P}_{\rm bg}/h\nu$ is the carrier generation rate due to background radiation.

Depending on which term in the denominator of Eq.(4.43) dominates detection will be thermal or background limited. Consider first the case where thermal noise dominates. Neglecting the 2$^{\rm nd}$ term in the denominator and setting the signal to noise ratio to unity we find for the minimum detectable power,

$$\mathcal{P}_{\rm min,th} = \sqrt{\frac{4k_BTB}{R_{\rm eff}}}\frac{h\nu}{{\rm e}\eta G}. \tag{4.44}$$

Using the parameters given in Table 4.5 for detector 5467 and using a 1 MHz bandwidth we find $\mathcal{P}_{\rm min,th} = 1.2\times10^{-6}$ W. This agrees well with the NEP calculated in Table 4.5 since we have here included the degradation due to the preamplifier noise. Thus at mW optical power levels detection is thermally limited.

It is instructive to calculate how large an optical power is required for detection to be background limited. The thermal carrier generation rate is unknown, but as a first approximation we may set it equal to the background rate $g_{\rm bg}$. The background rate is found by integrating the Planck distribution for thermal radiation times the spectral dependence of the photodetector sensitivity. As a rough estimate we may take the effective spectral bandwidth of the detector as 1 μm and using the curve given in [10] p.69, estimate $\mathcal{P}_{\rm bg} \sim 3\times10^{-5}$ W for our 1 mm^2 detectors. The background generation rate is then $g_{\rm bg} = 9.6\times10^{14}$ sec^{-1}. Equating the terms in the denominator of Eq. (4.43) gives

$$g^* = \frac{k_BT}{R_{\rm eff}{\rm e}^2G^2} - 2g_{\rm bg} \tag{4.45}$$

[3]The noise effective imput impedance is $R_{\rm eff,pa} = R_{\rm pa}10^{-NF/10}$, where NF is the noise figure in dB.

for the carrier generation rate g^* at which the signal dependent noise is equal to the thermal noise. We find $g^* = 3.2 \times 10^{20}$ sec^{-1} or, equivalently, for the corresponding optical power $\mathcal{P}^* = 10$ W. Since $\mathcal{P}^*$ is considerably greater than the damage level of the detector (which is 1 W) it is not possible to reach the signal noise limit in direct detection with the room temperature detectors we are using.

4.15.4 Heterodyne detection

In order to improve the sensitivity of the scattering diagnostic we adopt a heterodyne detection scheme. This means that the weak signal to be measured is combined with a much stronger local oscillator at the surface of the detector. Equation (4.39) for the signal to noise ratio then takes the form

$$z = \frac{\mathcal{I}_{\rm hd}^2}{I_{\rm lo}^2 + I_{\rm th}^2 + I_{\rm gr}^2 + I_{\rm pa}^2 + I_{1/{\rm f}}^2}, \tag{4.46}$$

with

$$\mathcal{I}_{\rm hd} = \frac{\eta {\rm e}}{h\nu}\eta_{\rm hd}\sqrt{\mathcal{P}\mathcal{P}_{\rm lo}}G, \tag{4.47}$$

$$I_{\rm lo}^2 = 4{\rm e}^2G^2B\frac{\eta\mathcal{P}_{\rm lo}}{h\nu}, \tag{4.48}$$

where $\mathcal{P}_{\rm lo}$ is the optical power of the local oscillator and $\eta_{\rm hd}$ is a factor less than one that accounts for the efficiency of the heterodyne mixing at the detector surface. $\eta_{\rm hd}$ requires some care to measure and we will assume that it has a numerical value of 1. Defining in the same fashion as above a carrier generation rate due to the local oscillator $g_{\rm lo}$, and again neglecting $1/f$ noise, we can rewrite Eq. (4.46) as

$$z = \frac{1}{4B}\frac{\eta_{\rm hd}^2{\rm e}^2G^2gg_{\rm lo}}{\frac{k_BT}{R_{\rm eff}} + {\rm e}^2G^2\left(g + g_{\rm lo} + g_{\rm bg} + g_{\rm th}\right)}. \tag{4.49}$$

As we found for the case of direct detection thermal noise is always dominant with the room temperature detectors. We can therefore simply write

$$\begin{aligned} z &= \frac{R_{\rm eff}}{4k_BTB}\eta_{\rm hd}^2{\rm e}^2G^2gg_{\rm lo}, \\ &= \frac{R_{\rm eff}}{4k_BTB}\left(\frac{\eta\eta_{\rm hd}{\rm e}G}{h\nu}\right)^2\mathcal{P}\mathcal{P}_{\rm lo} \end{aligned} \tag{4.50}$$

for the signal to noise ratio. We see that the power of the optical signal for which the signal to noise ratio is unity is inversely proprtional to the local oscillator power and is given by

$$\mathcal{P}_{\rm min,hd} = \frac{4k_BTB}{R_{\rm eff}}\left(\frac{h\nu}{\eta\eta_{\rm hd}{\rm e}G}\right)^2\frac{1}{\mathcal{P}_{\rm lo}}. \tag{4.51}$$

Setting $\mathcal{P}_{\rm lo}$ to 0.1 times the power at which detector damage occurs we find a minimum detectable optical power of 1.3×10^{-11} W, assuming a 1 MHz detection bandwidth. This is about five orders of magnitude less than the minimum detectable power found above for direct detection which demonstrates the superiority of the heterodyne configuration.

Nonetheless with a cooled infrared detector it is possible to achieve signal, or quantum, noise limited operation. In this case the dominant noise source is that generated by the local oscillator. Hence, from Eq. (4.49), the quantum limited signal to noise ratio is

$$z_{\rm ql} = \frac{1}{4B}\eta_{\rm hd}^2g. \tag{4.52}$$

Setting $z_{\rm ql}$ to unity we find the minimum detectable power in a 1 MHz bandwidth to be

$$\mathcal{P}_{\rm min,ql} = \frac{4Bh\nu}{\eta\eta_{\rm hd}^2} = 1.2\times10^{-13}\ {\rm W}. \tag{4.53}$$

detection scheme		bandwidth [MHz]		
		0.1	1.	10.
direct	$\mathcal{P}_{\min,\mathrm{th}}$ [W]	3.8×10^{-7}	1.2×10^{-6}	3.8×10^{-6}
power limited heterodyne	$\mathcal{P}_{\min,\mathrm{hd}}$ [W]	1.3×10^{-12}	1.3×10^{-11}	1.3×10^{-10}
quantum limited heterodyne	$\mathcal{P}_{\min,\mathrm{ql}}$ [W]	1.2×10^{-14}	1.2×10^{-13}	1.2×10^{-12}

Table 4.6: Minimum detectable power in Watts of the detectors and electronics installed at W7-AS for different detection limits and bandwidths.

In Table 4.6 we compare the minimum detectable powers for several different bandwidths for the cases of thermally limited direct detection, local oscillator power limited heterodyne detection, and quantum limited detection. We can conclude that a cooled infrared detector would increase the sensitivity by up to two orders of magnitude. This advantage has to be evaluated against the additional inconvenience, or cost, of cooled detectors. At the current time (november 1998) the limiting factor in our measurements at small k_{scat} is not the power level of the local oscillator, but rather amplification of the 40 MHz leakage signal due to parasitic scattering of the main beam into the local oscillator. Improvements to the beam scraper on the receiver table are intended to improve this situation.

Another issue is how much electronic amplification is needed to record a low-level signal $\mathcal{P}_{\min,\mathrm{hd}}$? The analog to digital electronics we are using have an input full range of 2 V_{pp}, or +10 dBm. An 8 bit conversion is made so the dynamic range is about 48 dB, and the minimum recordable input level is -38 dBm. The maximum electronic gain is 66 + 37.5 = 103.5 dB, thus the minimum recordable power level at the detector is about -142 dBm.

The photocurrent obtained for a minimum power $\mathcal{P}_{\min,\mathrm{hd}}$ is

$$\mathcal{I}_{\min,\mathrm{hd}} = \frac{\eta \mathrm{e}}{h\nu}\eta_{\mathrm{hd}}\sqrt{\mathcal{P}_{\min,\mathrm{hd}}\mathcal{P}_{\max,\mathrm{lo}}}G, \tag{4.54}$$

and the corresponding electrical power is

$$P_{\min,\mathrm{hd}} = \frac{V^2}{R_d} = \frac{(R_{\mathrm{eq}}\mathcal{I}_{\min,\mathrm{hd}})^2}{R_d} = \frac{R_{\mathrm{eq}}^2}{R_d}\left(\frac{\eta\eta_{\mathrm{hd}}\mathrm{e}G}{h\nu}\right)^2 \mathcal{P}_{\min,\mathrm{hd}}\mathcal{P}_{\max,\mathrm{lo}}. \tag{4.55}$$

Putting in the numbers for the 1 MHz bandwidth example we find $P_{\min,\mathrm{hd}} = -103.$ dBm. Thus at full electronic gain the minimum detectable signal will be amplified to about full range at the A/D converter.

A reasonable electronic amplification level in practice will be that for which the amplified thermal noise corresponds to say 4 bits after A/D conversion. This implies an electronic input gain setting of roughly 30 dB on the A/D card.

4.16 Correlation measurements

Photodetector signals

$$v_1(t) = v_{1E}(t)\cos(\Omega_D t) \tag{4.56}$$
$$v_2(t) = v_{2E}(t)\cos(\Omega_D t + \varphi) \tag{4.57}$$

Complex demodulated signals

$$v_{1c} = v_{1E}(t)e^{\imath\omega_D t} \tag{4.58}$$
$$v_{2c} = v_{2E}(t)e^{\imath(\omega_D t+\varphi)} \tag{4.59}$$

where $\omega_D = \Omega_D - \Omega_0$. Complex cross correlation can be defined as

$$\begin{aligned} R_{12}^{(c)}(\tau) &= < v_{1c}(t)v_{2c}^*(t-\tau) > \\ &= < v_{1E}(t)v_{2E}(t-\tau)e^{-\imath\varphi} > \\ &= R_{12}^{(E)}(\tau)e^{-\imath\varphi}, \end{aligned} \tag{4.60}$$

where the envelope correlation function is defined as

$$R_{12}^{(E)}(\tau) =< v_{1E}(t)v_{2E}(t-\tau) > . \tag{4.61}$$

Thus

$$|R_{12}^{(c)}|^2 = |R_{12}^{(E)}|^2. \tag{4.62}$$

The correlation function of the raw detector signals is

$$\begin{aligned} R_{12}(\tau) &= < v_1(t)v_2(t-\tau) > \\ &= < v_{1E}(t)v_{2E}(t-\tau)\cos(\Omega_D t)\cos(\Omega_D(t-\tau)+\varphi) > \\ &= \frac{1}{2} < v_{1E}(t)v_{2E}(t-\tau)\left(\cos[\Omega_D(2t-\tau)+\varphi] + \cos(\Omega_D\tau-\varphi)\right) > \\ &= \frac{1}{2}\left(R_{12}^{(E)}\cos(\Omega_D\tau-\varphi) + < v_{1E}(t)v_{2E}(t-\tau)\cos[\Omega_D(2t-\tau)+\varphi] >\right) \\ &\approx \frac{1}{2}R_{12}^{(E)}\cos(\Omega_D\tau-\varphi) \end{aligned} \tag{4.63}$$

where the last line follows from the narrow band signal assumption.

Thus

$$|R_{12}^{(c)}|^2 = \frac{4}{\cos^2(\Omega_D\tau-\varphi)}|R_{12}|^2 \tag{4.64}$$

Consider the case of a pure sinusoidal signal $v_{1E} = v_{2E} = 1$. Then

$$|R_{12}(\tau)|^2 = \frac{1}{4}\cos^2(\Omega_D\tau-\varphi), \tag{4.65}$$

so that

$$|R_{12}^{(c)}|^2 = |R_{12}^{(E)}|^2 = 1. \tag{4.66}$$

4.17 References

1. C. M. Surko and R. E. Slusher, "Study of the density fluctuations in the adiabatic toroidal compressor scattering tokamak using CO_2 laser", Phys. Rev. Lett. **37**, 1747-1750 (1976).

2. C. M. Surko and R. E. Slusher, "Study of plasma density fluctuations by the correlation of crossed CO_2 laser beams", Phys. Fluids **23**, 2425-2439 (1980).

3. J. Meyer and C. Mahn, "Microinstabilities in the Wendelstein VII A stellerator observed by CO_2 laser-light scattering", Phys. Rev. Lett. **46**, 1206-1209 (1981).

4. As discussed in C. Mahn, "Far forward scattering of CO_2 laser radiation by plasma density fluctuations in the W VII-A stellerator", Max-Planck-Institut für plasmaphysik, report 2/306, 1-38, (1990), the measurements of Meyer and Mahn[3] of small scale turbulence were attributable to corruption of the local oscillator beam.

5. H. U. Fahrbach, W. Köppendörfer, M. Münich, J. Neuhauser, H. Röhr, G. Schramm, J. Sommer, and E. Holzhauer, "Measurement of lower hybrid drift fluctuations in the boundary layer of a high-beta plasma by collective CO_2 laser light scattering", Nucl. Fusion **21**, 257-270 (1981).

6. TFR Group, A. Truc, and D. Grésillon, "Observation of fast and slow modes associated with ICRF heating in the TFR tokamak by CO_2 laser scattering", Nucl. Fusion **22**, 1577-1587 (1982).

7. D. E. Evans, E. J. Doyle, D. Frigione, M. von Hellermann, and A. Murdoch, "Measurement of long wavelength turbulence in a tokamak by extreme far forward scattering", Plasma Phys. **25**, 617-640 (1983).

8. M. von Hellermann and E. Holzhauer, "Far forward scattering from plasma fluctuations using a detector array and coherent signal processing at 10 μm", IEEE Trans. Plasma Sci. **12**, 5-11 (1984).

9. A. Truc, A. Quéméneur, P. Hennequin, D. Grésillon, F. Gervais, C. Laviron, J. Olivain, S. K. Saha, and P. Devynck, "ALTAIR: An infrared laser scattering diagnostic on the TORE SUPRA tokamak", Rev. Sci. Instrum. **63**, 3716-3724 (1992); P. Devynck, X. Garbet, C. Laviron, J. Payan, S. K. Saha, F. Gervais, P. Hennequin, A. Quéméneur, and A. Truc, "Localized measurements of turbulence in the TORE SUPRA tokamak", Plasma Phys. Control. Fusion **35**, 63-75 (1993).

10. E. L. Dereniak and G. D. Boreman, *Infrared detectors and systems*, (John Wiley & Sons, Inc., New York, 1996).

Chapter 5

Reference Information

5.1 Physical quantities

Plasma quantities:

$$\begin{aligned} \lambda_D &= \left(\frac{\epsilon_0 k_B T_e}{e^2 n_e}\right)^{1/2} \text{ m} \\ \omega_{pe} &= \left(\frac{n_e e^2}{\epsilon_0 m_e}\right)^{1/2} \text{ s}^{-1} \\ v_{te} &= \underline{k_B T_e}^{1/2} = \lambda_D \omega_{pe} \text{ m/s} \\ \omega &= \frac{eB}{m} \text{ s}^{-1} \\ \rho &= \frac{v}{\omega} = \frac{mv}{eB} \text{ m} \end{aligned} \tag{5.1}$$

Fundamental quantities:

$$\begin{aligned} c &= 2.9979 \times 10^8 \text{ m/s} \\ k_B &= 1.381 \times 10^{-23} \frac{\text{J}}{\text{K}} \\ &= 8.617 \times 10^{-5} \frac{\text{eV}}{\text{K}} \\ \hbar = \frac{h}{2\pi} &= 1.055 \times 10^{-34} \text{ Js} \\ \text{e} &= 1.602 \times 10^{-19} \text{ C} \\ m_e &= 9.1083 \times 10^{-31} \text{ kg} \\ m_e c^2 &= 0.511 \text{ MeV} \\ m_p &= 1.672623 \times 10^{-27} \text{ kg} \\ m_p c^2 &= 938.5 \text{ MeV} \\ m_n &= 1.674929 \times 10^{-27} \text{ kg} \\ m_n c^2 &= 938.? \text{ MeV} \\ \epsilon_0 &= 8.854 \times 10^{-12} \text{ F/m} \\ \mu_0 &= 4\pi \times 10^{-7} \frac{\text{H}}{\text{m}} \\ Z_0 &= 377 \text{ H/m} \\ G &= 6.672 \times 10^{-11} \frac{\text{m}^3}{\text{s}^2\text{kg}} \\ N_\text{A} &= 6.022 \times 10^{23} \frac{1}{\text{mol}} \end{aligned} \tag{5.2}$$

dBm	$V_{\rm rms}$	$V_{\rm pp}$	P [mW]
+10	0.71	2.01	10.
+3	0.32	.91	2.0
0	0.225	.64	1.0
-3	0.160	.45	.50
-10	0.071	.20	.10
-20	0.0225	.064	0.01

Table 5.1: Conversion from dBm to V for 50 Ω systems. The peak-to-peak voltage is related to the root-mean-square voltage by $V_{\rm pp} = 2\sqrt{2}V_{\rm rms}$.

Conversion between different systems of units

$$\begin{aligned}
1\text{ J} &= 10^7\text{ erg} \\
1\text{ eV} &= 1.6\times10^{-19}\text{ J} \\
1\text{ newton} &= 10^5\text{ dyne} \\
1\text{ volt} &= \frac{10^6}{c[\text{m/s}]}\text{ statvolt} \\
1\text{ ohm} &= 1.139\times10^{-12}\text{ s/cm} \\
1\text{ coulomb} &= 10\ c[\text{m/s}]\text{ statcoulomb} \\
1\text{ farad} &= 0.899\times10^{12}\text{ cm} \\
1\text{ tesla} &= 10^4\text{ gauss} \\
1\text{ henry} &= 1.113\times10^{-12}\text{ s}^2/\text{cm} \\
1\text{ tesla} &= 1\text{ weber/m}^2 \\
1\text{ gauss} &= 1\text{ oersted}
\end{aligned}$$

Some useful numerical values:

$$\begin{aligned}
k_BT &= 4.14\times10^{-21}\text{ J} = 0.026\text{ eV at room temperature (300K)} \\
h\nu &= 1.87\times10^{-20}\text{ J} = 0.117\text{ eV at } \lambda = 10.6\ \mu\text{m}
\end{aligned}$$

5.2 dBm's

The value in dBm of a power P is

$$P[dBm] \equiv 10\log_{10}\frac{P[\text{W}]}{0.001}. \tag{5.3}$$

Some handy rules of thumb are 3 dB is a factor of 2 in power and 10 dB is a factor 10 in power (6 dB gives a factor 2 in voltage and 20 dB gives a factor 10 in voltage).

The conversion between dBm and voltage levels depends on the choice of resistance. Some useful conversions are given in Table 5.1 for 50 Ω systems.